5.3

EXAMINING IN-CLOUD CONVECTIVE TURBULENCE IN RELATION TO TOTAL LIGHTNING AND THE 3D WIND FIELD OF SEVERE THUNDERSTORMS

Sarah Al-Momar[1,2]*, Wiebke Deierling[2], John Williams[2], and Eric Hoffman[1]

[1]Plymouth State University, Plymouth, New Hampshire
[2]National Center for Atmospheric Research (NCAR), Boulder, Colorado

1. INTRODUCTION

Experiencing atmospheric turbulence is a relatively common phenomenon for many airline passengers. Light to moderate turbulence can cause discomfort; however, moderate or greater (MoG), turbulence can lead to injury or even damage an aircraft. A study of National Transportation Safety Board data concerned with weather related commercial airline accidents listed turbulence as a cause or factor ~70% of the time (Eichenbaum 2000, Williams 2013). Kaplan et al. also showed that of 44 cases of severe turbulence resulting in passenger injury, 86% occurred within 100 km of deep convection (2005). Analysis of past data also showed that of all aviation accidents relating to turbulence, an estimated 60% were associated with thunderstorms (Cornman and Carmichael 1993, Williams 2013). This type of turbulence is known as convectively induced turbulence (CIT). Although there are many types of turbulence, previous studies indicate that CIT is the culprit for the majority of weather related commercial aviation accidents.

In-cloud CIT is dependent upon the in-cloud dynamics of a thunderstorm, such as convective updrafts and downdrafts and the shears that they produce (Lane et al. 2012). Since lightning also depends on convective updrafts, a relationship has been established between in-cloud CIT and total lightning. Precipitation based non-inductive charging is thought to significantly contribute to thunderstorm electrification (Reynolds et al. 1957; Saunders et al. 1991; Saunders and Peck 1998; Takahashi and Miyawaki 2002). The non-inductive charge mechanism involves collisions between ice hydrometeors, particularly in a mixed phase (0ºC to -40ºC) environment, within a robust updraft (greater than 6 ms^{-1}). These hydrometeor interactions can lead to strong enough electrification to facilitate lightning (Deierling and Petersen 2008). The updraft also serves as a generator of charge since it allows for the development of condensate and enhances collisions at updraft boundaries. Wiens et al. (2005) observed that as updrafts intensify, graupel echo volume and total flash rate increase, followed by an increase in the hail echo volume. Thus, higher radar reflectivity exceeding values of 35 or 40 dBZ at temperatures below freezing (e.g. Buechler and Goodman 1990) are a good indicator of an area where riming hydrometeors are developing within a strong updraft and by non-inductive charging, electrifying a storm.

By researching this process and its relationship with in-cloud CIT, the ability to identify in-cloud CIT and its intensity could be improved with the use of real-time lightning data. Radar is currently the primary CIT identification tool; thus, in areas of little radar coverage, such as over oceans, detection of CIT is exceedingly difficult. Although some airplanes have onboard radar, air traffic control does not have access to this data, complicating communication and decision making. Satellite imagery is also useful to identify overshooting tops and gravity waves, but provides little insight on in-cloud CIT and its severity (Williams 2013).The upcoming launch of the GOES-R (Geostationary Operational Environmental Satellite R-Series) would be instrumental in the identification of in-cloud CIT since this satellite will be equipped with a Geostationary Lightning Mapper (GLM), making nearly hemispheric lightning data readily available. Continued research of in-cloud CIT and lightning is needed to determine if lightning can be used as an accurate indicator of turbulence and its severity.

Bruning and MacGorman (2013) suggest that electric and kinematic motions are related and that electrical energy may be driven by convective turbulence. As charged particles move throughout a thunderstorm, turbulent eddies can help shape the charge structure and distribution. Bruning and

*Corresponding author address: Sarah Al-Momar, Dept. of Atmospheric Science & Chemistry, Plymouth State University, MSC #48, 17 High St., Plymouth, NH 03264; e-mail: sa1010@plymouth.edu

MacGorman (2013) hypothesize that in the highly turbulent core of a thunderstorm, multiple charge regions or pockets can develop and support the development of frequent, short flashes. In the anvil region, the charge structures are more uniform and horizontally stratified. This supports the development of less frequent, larger flashes. They found that flash size was generally smaller near convective updrafts and larger near stratiform or anvil regions of a thunderstorm (Bruning and MacGorman 2013; Carey et al. 2005; Kuhlman et al. 2009; Weiss et al. 2012). Bruning and MacGorman (2013) also showed that higher flash extent densities and smaller mean flash areas often occurred near a storm's updraft. This region also tended to be an area of high flash origin density and turbulence (Bruning and MacGorman 2013; Calhoun et al. 2013). Downwind, near the stratiform and anvil regions of a thunderstorm, the opposite occurred: flash extent density was lower, mean flash area was higher, and flash origin density was lower. Bruning and MacGorman (2013) conclude that continued research of 3D lightning data, as well as 3D kinematic structure, would enhance their findings and operational understandings of storm dynamics.

To better understand the relationships between in-cloud CIT and total lightning, this study will compare Lightning Mapping Array flash characteristics and NCAR/NEXRAD Turbulence Detection Algorithm estimated eddy dissipation rate to a storm's 3 dimensional wind field derived from a dual-Doppler synthesis. The dual-Doppler wind synthesis can be performed when a storm is located within the ranges of two or more radars (Dowell and Shapiro 2003). An explanation of data sources, the methods used to compute the dual-Doppler analysis, and the methods of comparison between the various data sources are described in Section 2. An overview of the case is presented in Section 3, followed by the results in Section 4. Section 5 discusses these results and lastly, Section 6 summarizes the findings.

2. DATA AND METHODOLOGY

2.1 *Radar data collection and processing*

This study used radar data from two different radars for the dual-Doppler analysis. The first was the Colorado State University-University of Chicago and Illinois State Water Survey (CSU-CHILL) radar, located in Greeley, Colorado, which is a dual-polarized and dual-wavelength instrument, transmitting in both S- and X- band (Colorado State University). The second radar was the Denver, Colorado (KFTG), S-band, NEXRAD. Although KFTG has now been upgraded for dual-polarization (September 2012), the case selected for this study occurred prior to the upgrade. For both radars, we unfolded and checked the velocity data for quality assurance, including the removal of ground clutter, side lobes, and multiple trip echoes using NCAR's SOLO II software.

Once filtered, the radar data were gridded from a polar coordinate system to a Cartesian coordinate system. Radx2Grid interpolated the radar data using bounded, linear interpolations from neighboring gates and converted them into latitude-longitude grid boxes of equal size (http://box.mmm.ucar.edu/pdas/pdas.html#overview; http://www.ral.ucar.edu/projects/titan/docs/radial_formats/radx.html#top). NCAR's Custom Editing and Display of Reduced Information in Cartesian Space (CEDRIC) was used to perform the dual-Doppler synthesis.

Three constraints are used by CEDRIC when doing a dual-Doppler synthesis:

$$\boldsymbol{r_1} * \mathbf{v} = \sin\alpha_1 \cos\Phi_1 u + \cos\alpha_1 \cos\Phi_1 v + \sin\Phi_1 w = v_r^1 - \sin\Phi_1 w_t \equiv V_1 \qquad (1)$$

$$\boldsymbol{r_2} * \mathbf{v} = \sin\alpha_2 \cos\Phi_2 u + \cos\alpha_2 \cos\Phi_2 v + \sin\Phi_2 w = v_r^2 - \sin\Phi_2 w_t \equiv V_2 \qquad (2)$$

$$du/dx + dv/dy + dw/dz + 1/p*dp/dz = 0 \qquad (3)$$

in which the sub/superscripts "1" and "2" refer to each radar; $\mathbf{r} = \sin\alpha \cos\Phi\mathbf{i} + \cos\alpha \cos\Phi\mathbf{j} + \sin\Phi\mathbf{k}$ is the unit vector for the radar beam's direction; $\mathbf{v}(x, y, z) = u\mathbf{i} + v\mathbf{j} + w\mathbf{k}$ is the 3D wind vector at x, y, z in a Cartesian coordinate system; u, v, and w are Cartesian components of the wind vector; α is the azimuth angle; Φ is the elevation angle; v_r is the Doppler radar measured radial velocity; w_t is the fall speed of the hydrometeors; and V is the radial velocity of air in the horizontal (Dowell and Shapiro 2003). These last three variables are related by the following equation:

$$V = v_r - w_t \qquad (4)$$

where w_t is a function of reflectivity and height (Marks and Houze 1987). Equation 3 is the anelastic mass continuity equation which allows for the estimates of vertical velocity to be possible. Thus, to complete a dual-Doppler analysis, one must solve equations 1-3 for u and v and integrate the continuity equation to find w (Dowell and Shapiro 2003). This integration, however, can cause errors, such as reduced horizontal resolution from smoothing and a misalignment of convergent-divergent couplets due to the time lag between radar tilts (Matejka and Bartels 1998). A variational integration method, using a combination of upwards and downwards integration, was ultimately used in this study, although other integration methods were examined.

2.2 *NCAR/NEXRAD Turbulence Detection Algorithm (NTDA)*

We quantified turbulence in this study with NTDA estimated eddy dissipation rate (EDR), constructed into a 3D mosaic from KFTG and other NEXRADs (see Williams et al. 2006 for a full description). Combining reflectivity, radial velocity, and spectrum width from multiple NEXRADs with a fuzzy-logic algorithm, the NTDA can mosaic estimated EDR for every range-azimuth-elevation point in a volume scan (Williams et al. 2006). Radar censoring removed non-meteorological targets, such as ground clutter, by assigning a quality control “confidence” value to each spectrum width measurement. The final EDR values are confidence-weighted means. Turbulence thresholds were assigned to EDR volumes from 0.15-0.22 $m^{2/3}$ s^{-1}, 0.22-0.34 $m^{2/3}$ s^{-1}, and 0.34+ $m^{2/3}$ s^{-1} to represent light, moderate, and severe turbulence, respectively (adapted from Sharman et al. 2014).

2.3 *Lightning Mapping Array (LMA)*

This study uses flash characteristics from the Colorado LMA to compare with the results of the dual-Doppler synthesis and infer the storm’s electrification state in relation to its 3D wind field. Developed by the New Mexico Institute of Mining and Technology, the LMA is a time-of-arrival system that detects the 3D location of very high frequency (VHF) sources emitted from lightning discharges at around 60-66 MHz (Thomas et al. 2004). This system maps entire flash structures in order to examine how lightning varies in space and time.

LMA VHF sources were used to derive several flash characteristics following Bruning and MacGorman (2013) and Bruning (2014). This included VHF source densities, flash extent densities, mean flash area, and flash initiation densities. VHF source densities show the sum of all VHF sources associated with flashes. Flash extent densities are the number of flashes that pass through each grid box and thus, indicate regions of a storm that are energetically favorable for lightning flashes (Bruning 2014). Mean flash area shows the average area of all flashes in a grid box by dividing the sum of all flash areas by the flash extent density for each grid box (Bruning 2014). This variable highlights regions of infrequent, but large flash areas and frequent, but small flash areas such as in the anvil and convective core regions respectively. Lastly, flash initiation density was computed, where each grid box containing the first VHF source per flash is counted (Bruning 2014).

2.4 *Methodology*

Storm volume, time-height plots were created to investigate storm volume, spatial and temporal relationships between reflectivity, EDR, and VHF source densities. At each point in time, the color gradient shows how many grid boxes in the storm’s volume were above a specific threshold. Reflectivity greater than 35 dBZ was chosen as a threshold since it has been shown to correlate with the presence of graupel (Straka et al. 2000, Deierling et al. 2008). The presence of this riming hydrometeor on radar has been shown to correspond to the occurrence of lightning (Buechler and Goodman 1990, Saxen et al. 2008, Mosier et al. 2011). Other plots include VHF source densities greater than 1 and the aforementioned EDR thresholds of light, moderate, and severe turbulence.

Each time-height plot was also normalized based on the size of the domain used, which fluctuated with storm size. This domain captured the entire storm echo, including convective and stratiform regions, which sometimes included pulses of other storms in close proximity to the main storm of interest. Data were only used within the range of the LMA (~200 km).

3. STORM DESCRIPTION

The atmospheric conditions from 6-8 June 2012 were conducive for severe convective storms in the Front Range and eastern Colorado. A longwave trough in the upper troposphere was located over the western U.S. In response to the synoptic scale forcing associated with the longwave trough and southwesterly flow aloft, a lee trough was located along the Front Range. To the east of the surface lee trough a narrow band of low-level moisture extended northward from Texas into eastern Colorado and southeastern Wyoming.

On both June 6th and 7th, convection developed just along and east of the Rockies in the late afternoon and moved into the Plains as the evening progressed. The convective storms on June 7th were chosen for this study because severe thunderstorm cells were observed in the dual- Doppler domain between the CHILL and KFTG radars.

From 1200 UTC 7 June 2012 to 0000 UTC 8 June 2012, a shortwave upper-tropospheric trough over the Four Corners region lifted northeastward and weakened as it moved to Wyoming and southern Montana. In response to this shortwave trough, the lee trough strengthened by 0000 UTC 8 June 2012 into a closed surface lee cyclone in central Colorado (Fig. 1). Southeasterly flow just to the northeast of the lee cyclone allowed moisture to increase in northeastern Colorado (surface Td of 10–13°C, not shown).

The 0000 UTC 8 June sounding from Denver (Fig. 2) indicated steep mid-level lapse rates. These lapse rates combined with the increased low-level moisture created an unstable atmosphere with surface based convective available potential energy in excess of 3000 J kg^{-1}. The sounding shows that the surface and lowest-level winds were from the north-northeast with significant directional shear as the winds veer to the southeast by 900 hPa, to the southwest at 850 hPa and around to the west northwest above 600 hPa. The magnitude of the winds in the middle and upper-troposphere are weak (<25 m s^{-1}), but the directional change in the wind allows for moderately high values of bulk shear (6 m s^{-1} for the 0–1 km layer, and 15 m s^{-1} for the 0-6 km layer). The relatively strong instability combined with moderate shear and a veering wind profile provided an environment favorable for the development of supercell thunderstorms.

Isolated convective cells began to develop in the lee of the Rockies between 2100 and 2200 UTC 7 June 2012. The cells that are analyzed in this study developed just to the east-southeast of the KFTG radar. At about 2200 UTC the first convective cluster (0.5 deg reflectivity >35 dBZ) developed in eastern Adams and Arapahoe counties (hereafter referred to as the "northern cell," Fig. 3A) and moved slowly to the northeast. By 2230 UTC, these early cells organized into a larger cluster located in eastern Adams county (Fig. 3B). At this time, new small cells began to form southwest of the original cells in central Arapahoe county (hereafter referred to as the "southern cell"). By 2258 UTC the northern cell was moving out of the right dual Doppler lobe into southern Morgan county (Fig. 3C,D), the southern cell was located over eastern Arapahoe county and developed a well defined mesocyclone. By 2330 UTC (Fig. 4A), the original reflectivity core and the mid-level rotation associated with the southern cell weakened. However, by 2358 UTC (Fig. 4B), a new reflectivity core and a new mesocyclone developed to the south of the storm. The southern cell continued evolve and to move slowly southward exiting the dual-Doppler domain by 0030 UTC 8 June 2012. After leaving the dual-Doppler domain, the southern cell continued to produce severe weather until at least 0700 UTC 8 June (4C). The analysis of turbulence, LMA lightning, and 3D wind structure will focus on the period 2130 UTC 7 June to 0030 UTC 8 June when both the northern cell and southern cell were in the eastern dual-Doppler lobe. Additional analysis of the turbulence and lightning structure is presented through 0700 UTC as the southern cell moved slowly southward.

4. RESULTS

4.1 *Analysis of electrical and kinematic storm properties*

All intensities of NTDA estimated EDR are first detected around 2140 UTC between 15,000-27,000 feet. Severe turbulence is shown near the top of this range situated over the convective cores. It eventually spreads upward from near the melting level and expands horizontally downstream in a "V" shape. Near the cloud tops, turbulence is nearly all severe by 2150 UTC. This trend continues throughout both storm's life cycles, an example is depicted in Fig. 5. The LMA detects lightning flashes from 2200 UTC on. Similar to the turbulence, the VHF sources appear to be concentrated near the cores, but also stretch downstream into the stratiform region (See Fig. 5).

The northern cell intensifies quicker than the southern cell and progresses northeastward. At 2326 UTC, the northern cell produces severe wind gusts of up to 60 knots and at 2330 UTC, hail of up to 2.75 inches in diameter. By 2345 UTC, the storm begins to weaken making the southern cell the more dominant storm and at 0020 UTC on 8 June 2012, the northern cell begins to merge with larger cells to the north.

The time-height plots of the northern cell show reflectivity greater than 35 dBZ pulsing from about 2155-2318 UTC (Fig. 6). Just above these towers, from 21,000-40,000 feet, high concentrations of moderate turbulence form. High concentrations of severe turbulence also begin around 19,000 feet, near the melting level, and then spread upward above the towers, concentrated between 27,000 and 43,000 feet. These high concentrations of turbulence appear to be capped by the tropopause, which occurred between 45,000-50,000 feet on this day according to National Weather Service soundings. Soon after this initial increase in severe turbulence volume, VHF source densities increase rapidly. Similar patterns of turbulence increasing rapidly followed by a sharp increase in VHF sources are also seen at 2216 UTC and 2356 UTC. The northern cell experiences a sharp drop off in all intensities of turbulence, VHF source densities, and reflectivity by 2325 UTC before the storm pulses again around 2359 UTC.

From 2305-2310 UTC, a bounded weak echo region and lightning hole were present in the reflectivity and LMA data indicating a strong updraft in the southern cell (Fig. 7). This storm produced one tornado at 2321 UTC and another tornado at 0018 UTC on 8 June 2012 (Storm Prediction Center). Throughout the southern cell's life cycle, it produced a total of four tornadoes (2321, 0018, 0100, and 0146 UTC), severe hail of up to 2.5 inches in diameter (2310, 2340, 0020, 0032, 0238, and 0257 UTC), and severe wind gusts of up to 75 knots (0201 and 0436 UTC) (Storm Prediction Center). At 0140 UTC, the stratiform region of the southern cell begins to move out of the LMA's far eastern range. By 0210 UTC, it begins to exit the LMA's southernmost range and at 0305 UTC, the convective core begins to move out of this range as well. At least partial flash extent (for the parts of the storm still in the LMA range) is derived until at least 0625 UTC with severe turbulence lasting until 0655 UTC. This long-lived storm continues to progress until about 0700 UTC on the 8th where it weakens substantially.

At 2356 UTC, the time-height plots show the southern cell reflectivity volume above 35 dBZ increasing relatively quickly (Fig. 8). Unlike early in the storm's evolution where increases in VHF source densities trailed increases in turbulence, all levels of turbulence as well as VHF source densities increase at about the same time. This is seen again near 0252 UTC.

Near 0048 UTC, severe turbulence extends upward rapidly to 63,000 feet. The severe turbulence volume jumps above 60,000 feet four more times in the southern cell's life cycle (about 0124, 0217, 0253, and 0302 UTC). Although some of these sharp increases in height appear to correspond with overshooting tops shown in the reflectivity volume time-height plot, the plots do not glean at any other relationships.

MoG turbulence volumes decrease rapidly around 0438 UTC, the same time VHF source densities and radar reflectivity volume above 35 dBZ decrease. Light turbulence, however, increases at this time. This may be due to the weakening storm's downdrafts and gust fronts spurring the development of light turbulent eddies. Note that the accuracy of the VHF source densities at this time is compromised since the convective core is moving out of the range of the LMA.

For both storms, when comparing the maximum values of reflectivity, EDR, and concentration of VHF source densities spatially, EDR is always concentrated near the cloud tops (~33,000 feet and above), reflectivity is near the cloud bases (~33,000 feet and below), and VHF source densities are sandwiched in between (~12,000-54,000 feet; Fig.9). There also appears to be maximums in EDR near the base of the storms (~15,000 feet and below). This is likely due to downdrafts and gust fronts creating low-level, in-cloud turbulence as well as the natural cascade of turbulence as more severe turbulence weakens to low turbulence. All levels of EDR (light, moderate, and severe) also have an overall downward trend as turbulence is pushed lower with height throughout the storm's life. This is most visible when examining the bottom half of the light or greater EDR time-height plot for the southern cell (Fig. 10). One explanation for this downward movement of turbulence could be the shortwave trough that was moving through the region. As the trough progressed eastward, the tropopause height likely fell, causing the trapped turbulence to be pushed farther down as well.

4.2 *Charge structure and evolution*

Based on a LMA flash analysis that was preformed, the storm has an inverse polarity charge structure with a main positive charge region below a negative charge region early in the storm's life cycle. By 2256 UTC, the storm begins to split into the two dominant cells (northern and southern). As both storms strengthen, the polarities become more complicated with multiple charge regions. Flashes originating near the convective core appear to be shorter than those originating downstream in the more stratiform regions and often occur near reflectivity and turbulence vertical gradients (see Figs. 11 and

12). Near 0140 UTC, the southern cell begins to move out of the LMA range and thus the flashes suffer from a reduced resolution.

4.3 *Dual-Doppler Analysis*

Due to limitations in the coverage of both radars, the dual-Doppler analysis only covers most time periods from 2235-0003 UTC. Early during this time frame, from 2235-2239 UTC, reflectivity indicates that the northern cell is the dominate storm. At 3 km, there is a defined notch in the 35 dBZ echo associated with low-level convergence and southeasterly inflow into the storm (see Fig. 13). At 6.5 km, a velocity couplet indicates the presence of a mid-level mesocyclone with vertical velocity (W) around 20 m/s (see Fig. 14). Vorticity shows that the cyclonic turning of the inflow (now from the southwest) transitions into an anticyclonic turn as the wind makes a “S” shape within the storm. Flow outside all of the storms also appears to be diffluent as it splits around the storm and then converges downstream, behind the storm. The updraft is maximized around 9 km at ~25 m/s (not shown). At 12 km, divergence is dominating and the downstream convergence is maximized, producing straight northerly flow (see Fig. 15).

Although the southern cell is not as impressive as the northern cell on reflectivity, other variables show that it is rapidly intensifying and may be the more severe storm. There is still a large area of low-level convergence and at mid-levels, there is a defined area of cyclonically turning inflow winds, velocity couplet, and robust updraft of ~26 m/s (see Figs. 13 and 14). This updraft is maximized a little higher at 10.5 km, with values around 34 m/s (not shown). At 12 km, there is stronger divergence above the southern cell’s updraft and signs of a back-sheared anvil (see Fig. 15). W is still >29 m/s at this height as well. Beginning to form downstream of both storms are confluent lines with straight northerly flow. Along these lines are couplets of upward/downward, divergent/convergent, and cyclonic/anticyclonic flow.

Not long after this time period, from 2307-2312 UTC, the northern cell is visibly weaker on reflectivity while the southern cell is clearly dominant. The southern cell has a well defined hook echo and strong low-level cyclonic rotation and convergence (see Fig. 16). A mesocyclone extends from around 3-8 km and at 6.5 km, the southern cell has broad, large scale rotation and the northern cell only has smaller pieces of its original updraft (see Fig. 17). The southern cell also has a stronger 12 km updraft of ~27 m/s (~38 m/s at 10 km) and widespread divergence associated with its updraft compared to the northern cell’s at the same height (see Fig. 18). Although these W values may seem high, an estimate of W using the most unstable CAPE from the 18 UTC sounding shows that Ws of up to 73 m/s were possible for the day. Flow continues to diverge around the storm’s core and converge downstream forming the confluent lines previously mentioned.

From 2344-2349 UTC, the northern cell has broken apart and has left the dual-Doppler lobe. In contrast, the southern cell is still severe and is just starting to reach the southern edge of the dual-Doppler lobe. On reflectivity at 6.5 km, an elongated appendage extends southward and a new mesocyclone with W~27m/s is developing here (see Fig. 19). Higher aloft at 12 km, the updraft is up to ~32 m/s and the confluent lines appear to be moving southward (see Fig. 20).

4. DISCUSSION

When examining the overall relationship between the LMA flash characteristics, turbulence, and the updrafts of these storms, a number of patterns arise. As shown in Fig. 21, high flash extent densities, flash initiation densities, and VHF source densities appear to occur near the convective cores of the storms. High turbulence is also present in this region. Near the stratiform regions, these flash characteristic densities decrease rapidly, but mean flash area increases. Turbulence severity increases with height and following the divergent motions of the ambient flow around the storm’s updraft, maxima in turbulence appear to surround the updraft (see Fig. 22). A lightning hole can be seen surrounding the updraft and is in approximately the same region as the turbulence hole.

From 2305-2309 UTC, the mesocyclone in the southern cell transitions as a new mesocyclone develops further south. Fig. 23 shows two lightning holes as this phase in the storm’s life cycle occurs. Still, flash extent density, initiation density, and VHF source density maximize in the convective core, while the mean flash area maximizes in the stratiform regions. Higher aloft at 12 km, two turbulence holes coincide with the current updraft and its predecessor (see Fig. 24). Although the lightning holes do not align with the turbulence holes at this time period, by 2345-2350 UTC they do (see Fig. 25). During this time period, the old mesocyclone does not have much of a signature in the turbulence data, but a small lightning hole lingers. However, the stronger and more defined lightning and turbulence holes align with the current updraft to the south. This is indicative of the strong mesocyclone, with vertical velocities of over 30 m/s.

The previously mentioned confluent lines do not appear to correspond to any increases in turbulence or lightning activity. Although some less frequent flashes do occur in regions of higher turbulence in the anvil region, these regions do not seem to correlate with the confluent lines. Given the sharp gradients in vertical motion and vorticity the dual-Doppler analysis indicated, high shears should be expected in that region, thus it is puzzling as to why a response in turbulence is not indicated in the NTDA estimates. More research is needed to examine this issue.

6. CONCLUSIONS

In order to assess the use of total lightning as an indicator of convectively induced turbulence, this study investigated the kinematics, lightning, and turbulence produced by a severe thunderstorm over northeastern Colorado from 7th-8th June 2012. For this case, increases of turbulence and lightning occurred within a few minutes of each other. MoG turbulence appeared to originate near the convective core of the storms and then extend upward and outward in a “V” shape. Lightning activity also had a maximum near the updraft and convective cores. Consistent with past research, short, but frequent flashes occurred in this region while long, but less frequent flashes occurred in the stratiform regions. In this case study, for the convective region, lightning coincides with areas of MoG turbulence.

Throughout the storm’s life cycle, the ambient flow diverged around the storm. This led the turbulence maxima in the convective core to also diverge around the rotating updraft. A lightning hole was often collocated with this turbulence hole, indicating a bounded weak echo region and a robust updraft. Downwind of the storm, in the stratiform anvil regions, these winds converged and produced confluent lines with convergent/divergent and cyclonic/anticyclonic couplets. Although these lines look to be producing strong shears, little turbulence and lightning were associated with them.

The dual-Doppler plots introduced new variables to compare storm kinematics to lightning and turbulence. Although this study begins to look at possible relationships between these variables, more research is needed to solidify results. There is much to learn about how to further use this information to understand storm dynamics and use in an operational setting.

ACKNOWLEDGMENTS

Thank you to CSU-CHILL for providing the CHILL data, Jay Miller for help with the dual-Doppler analysis, Eric Bruning for his LMA algorithms and data, Jason Cordeira for coding help, Bob Sharman for his turbulence expertise and insight, the SOARS program and the Plymouth State University graduate program. This work was performed under the auspices of the Significant Opportunities in Atmospheric Research and Science Program. SOARS is managed by the University Corporation for Atmospheric Research and is funded by the National Science Foundation, the National Oceanic and Atmospheric Administration, the Cooperation Institute for Research in Environmental Science, the University of Colorado Boulder, and by the Center for Multiscale Modeling of Atmospheric Processes.

REFERENCES

Bruning, E. C., 2014: DC3 flash product data for select IOPs. 4 pp, [Available online at http://data.eol.ucar.edu/datafile/nph-get/353.201/DC3_flash_stats_documentation.pdf.]

Bruning, E. C. and D. R. MacGorman, 2013: Theory and observations of controls on lightning flash size spectra. *J. Atmos. Sci.*, **70**, 4012–4029. doi: http://dx.doi.org/10.1175/JAS-D-12-0289.1

Buechler, D. E., and S. J. Goodman, 1990: Echo size and asymmetry: Impact on NEXRAD storm identification. J. Appl. Meteor., **29,** 962 – 969.

Calhoun, K. M., D. R. MacGorman, C. L. Ziegler, and M. I. Biggerstaff, 2013: Evolution of lightning activity and storm charge relative to dual-Doppler analysis of a high-precipitation supercell storm. *Mon. Wea. Rev.*, **141**, 2199–2223. doi: http://dx.doi.org/10.1175/MWR-D-12-00258.1

Carey, L. D., M. J. Murphy, T. L. McCormik, and N. W. Demetriades, 2005: Lightning location relative to storm structure in a leading-line trailing stratiform mesoscale

convective system. *J. Geophys. Res*., **110**, D03105, doi:10.1029/2003JD004371.
Colorado State University, 2014: CSU-CHILL National Radar Facility. [http://www .chill.colostate.edu/w/CSU_CHILL.]
Cornman, L. B. and B. Carmichael, 1993: Varied Research Efforts Are Underway to Find Means of Avoiding Air Turbulence. ICAO Journal, **48**, 10-15.
Deierling, W., and W. A. Petersen, 2008: Total lightning activity as an indicator of updraft characteristics. J. Geophys. Res. **113**, D16210. doi:10.1029/2007JD009598
Dixon, M., EOL/RAL, cited 2014: Radx C++ Software Package for Radial Radar Data. [Available online at http://www.ral.ucar. edu/projects/titan/docs/radial_formats/radx .html#top.]
Dowell, D. C. and A. Shapiro, 2003: Stability of an iterative dual-Doppler wind synthesis in Cartesian coordinates. *J. Atmos. Oceanic Technol.*, **20**, 1552–1559. doi: http:// dx.doi.org/10.1175/ 1520-0426(2003) 020<1552:SOAIDW>2.0.CO;2
Eichenbaum, H., 2000: Historical overview of turbulence accidents. Rep. TR-7100/023-1, MCR Federal, Inc.
Federal Aviation Administration, 2014: Chapter 7. Safety of Flight. FAA Aeronautical Information Manual. [Available online at www.faa.gov/air_traffic/publications/ATpubs/AIM/.]
Kaplan, M. L., Huffman, A. W. Lux, K. M. Charney, J. J. Riordan, A. J. & Lin, Y.-L., 2005: Characterizing the severe turbulence environments associated with commercial aviation accidents. Part 1: a 44-case study synoptic observational analysis, Meteorology and Atmospheric Physics, **88,** 129–153.
Kuhlman, K. M., D. R. MacGorman, M. I. Biggerstaff, and P. R. Krehbiel, 2009: Lightning initiation in the anvils of two supercell storms. *Geophys. Res. Lett.*, **36**, L07802, doi:10.1029/ 2008GL036650.
Lane, T. P., R. D. Sharman, S. B. Trier, R. G. Fovell, J. K. Williams, 2012: Recent advances in the understanding of near-cloud turbulence. Bull. Amer. Meteor. Soc., **93,** 499–515. doi: http:// dx.doi.org/10.1175/BAMS-D-11- 00062.1
Marks, F. D. and R. A. Houze, 1987: Inner core structure of Hurricane Alicia from airborne Doppler radar observations. *J. Atmos. Sci.*, **44**, 1296–1317.doi: http://dx. doi.org/10.1175/1520-0469(1987)044< 1296:ICSOHA>2.0.CO;2
Matejka, T. and D. L. Bartels, 1998: The accuracy of vertical air velocities from Doppler radar data. *Mon. Wea. Rev.*, **126**, 92–117. doi: http://dx.doi.org /10.1175/1520-0493(1998)126<0092: TAOVAV>2.0.CO;2
MMM NCAR, cited 2014: Data Analysis Software. [Available online at http://box.mmm.ucar. edu/pdas/pdas.html#overview.]
Mohr, C. G., L. J. Miller, R. L. Vaughan, and H. W. Frank, 1986: The merger of mesoscale datasets into a common Cartesian format for efficient and systematic analyses. *J. Atmos. Oceanic Technol.*, **3**, 143–161.doi: http://dx. doi.org/10.1175/1520-0426(1986)003< 0143:TMOMDI>2.0.CO;2
Mohr, C. G., L. J. Miller and R. L. Vaughan, 1981: An interactive software package for rectification of radar data to three-dimensional Cartesian coordinates. *Preprints, 20th Conf. on Radar Meteor.*, Boston, MA, Amer. Meteor. Soc., 690-695.
Mosier, R. M., C. Schumacher, R. E. Orville, and L. D. Carey, 2011: Radar nowcasting of cloud-to-ground lightning over Houston, Texas. Wea. Forecasting, **26**, 199 – 212.
Reynolds, S. E., M. Brook, and M. F. Gourley, 1957: Thunderstorm charge separation. *J. Meteorol.*, **14,** 5, 163–178.
Saunders, C. P. R., W. D. Keith, and R. P. Mitzeva, 1991: The effect of liquid water content on thunderstorm charging. *J. Geophys. Res.,* **96,** 11,007–11,017.
Saunders, C. P. R., 1993: A review of thunderstorm electrification processes. J. Appl. Meteor., **32,** 642–655. doi:10.1175/ 1520-0450
Saunders, C. P. R., and S. L. Peck, 1998: Laboratory studies of the influence of the rime accretion rate on charge transfer during crystal/graupel collisions. *J. Geophys. Res.*, **103,** D12, 13,949–13,956.
Saxen, T. R., C. K. Mueller, T. T. Warner, M. Steiner, E. E. Ellison, E. W. Hatfield, T. L. Betancourt, S. M. Dettling, and N. A. Oien, 2008: The Operational Mesogamma-Scale Analysis and Forecast System of the U.S. Army Test and Evaluation Command. Part IV: The White

Sands Missile Range Auto-Nowcast System. J. Appl. Meteor. Clim., **47,** 1123–1139.

Sharman, R., L. Cornman, G. Meymaris, J. Pearson, and T. Farrar, 2014: Description and derived climatologies of automated in situ eddy dissipation rate reports of atmospheric turbulence. J. Appl. Meteor. Climatol. doi:10.1175 /JAMCD-13-0329.1, in press.

Storm Prediction Center, 2014: Severe Weather Events Archive 7 June 2012 [http://www.spc.noaa.gov/exper/archive/event.php?date=20120607].

Straka, J.M., D.S. Zrnic, and A.V. Ryshkov 2000: Bulk hydrometeor classification and quantification using polarimetric radar data: synthesis of relations. J. Appl. Meteor., **39,** 1341-1372.

Takahashi, T., and K. Miyawaki, 2002: Reexamination of riming electrification in a wind tunnel. *J. Atmos. Sci.,* **59**, 5, 1018–1025.

Thomas, R., P. R. Krehbiel, W. Rison, S. J. Hunyady, W. P. Winn, T. Hamlin, and J. Harlin, 2004: Accuracy of the lightning mapping array. *J. Geophys*. Res., **109**, D14207.doi:10.1029/ 2004JD004549

Weiss, S. A., D. R. MacGorman and K. M. Calhoun, 2012: Lightning in the anvils of supercell thunderstorms. *Mon. Wea. Rev.*, **140**, 2064–2079. doi: http://dx.doi.org/10.1175/MWR-D-11-00312.1

Wiens, K. C., S. A. Rutledge, S. A. Tessendorf, 2005: The 29 June 2000 supercell observed during STEPS. Part II: Lightning and charge structure. *J. Atmos. Sci.*, **62,** 4151– 4177.

Williams, J. K., L. B. Cornman, J. Yee, S. G. Carson, G. Blackburn, J. Craig, 2006: NEXRAD detection of hazardous turbulence. *44th Aerospace Sciences Meeting and Exhibit, Reno, NV*, AIAA, 1-16.

Williams, J. K., 2013: Using random forests to diagnose aviation turbulence. Machine Learning. doi: 10.1007/s10994-013-5346-7.

Vivekanandan, J., S. M. Ellis, R. Oye, D. S. Zrnic, A. V. Ryzhkov, J. Straka, 1999: Cloud Microphysics Retrieval Using S-band Dual-Polarization Radar Measurements. *Bull. Amer. Meteor. Soc.*, **80**, 381–388. doi: http://dx. doi.org/10.1175/1520-0477(1999)080<0381:CMRUSB>2.0.CO;2

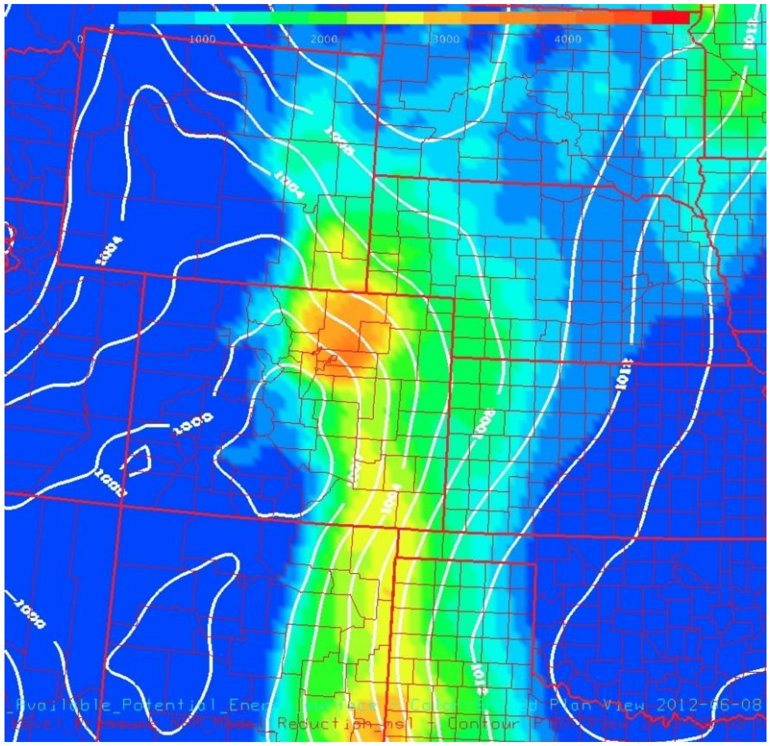

Fig. 1 North American Mesoscale (NAM) model 00 h forecast valid 0000 UTC 8 June 2012. Sea level pressure (hPa, white contours, interval = 2 hPa), and surface based CAPE (J kg^{-1}, color shaded).

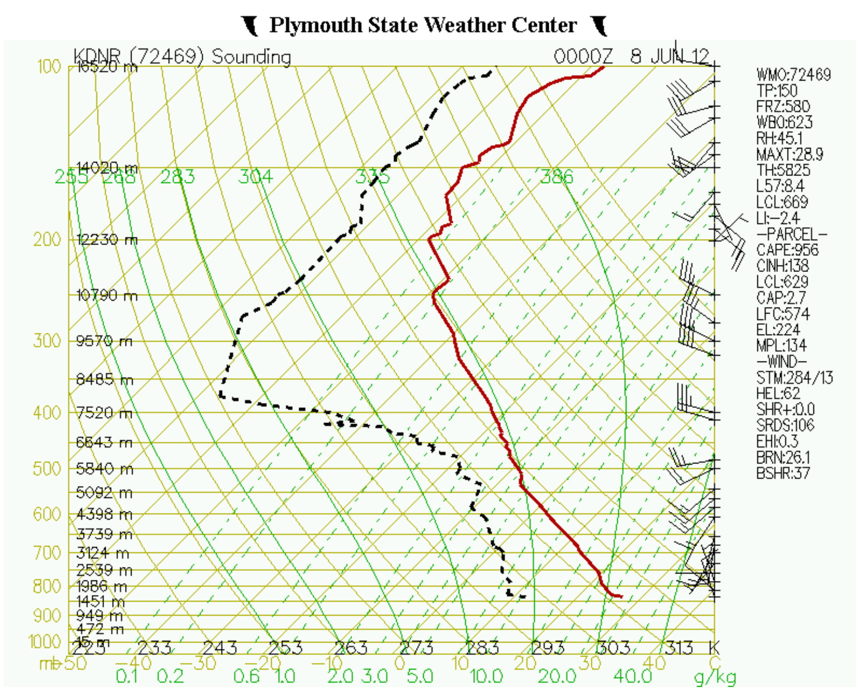

Fig. 2 Skew-T Log-P Diagram from KDNR at 0000 UTC 8 June 2012.

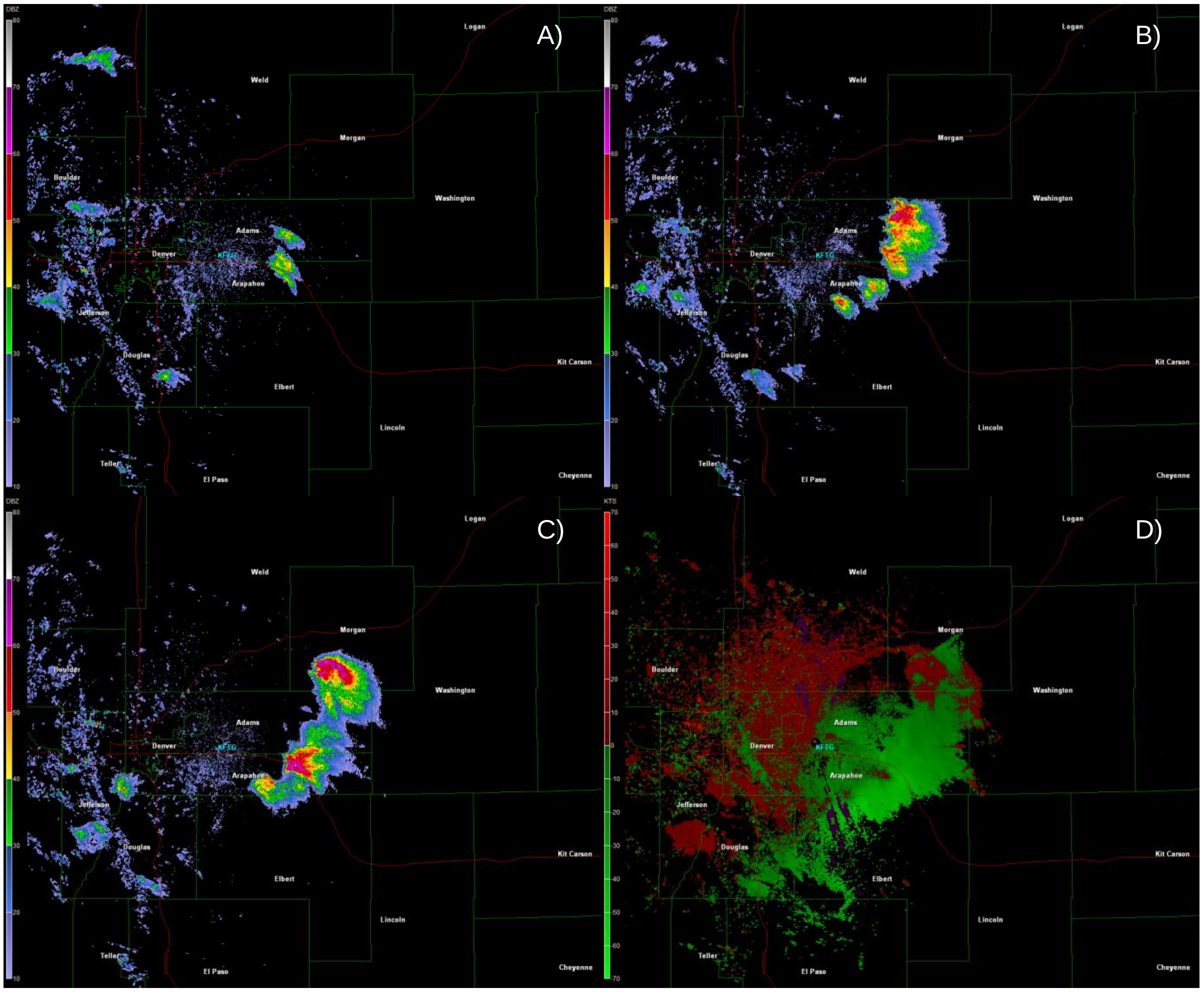

Fig. 3 KFTG 7 June 2012 radar 0.5 deg. radar reflectivity (dBZ): A) 2202 UTC; B) 2230 UTC; C) 2258 UTC; and D) 2258 UTC 0.5 deg. base radial velocity (m s^{-1})

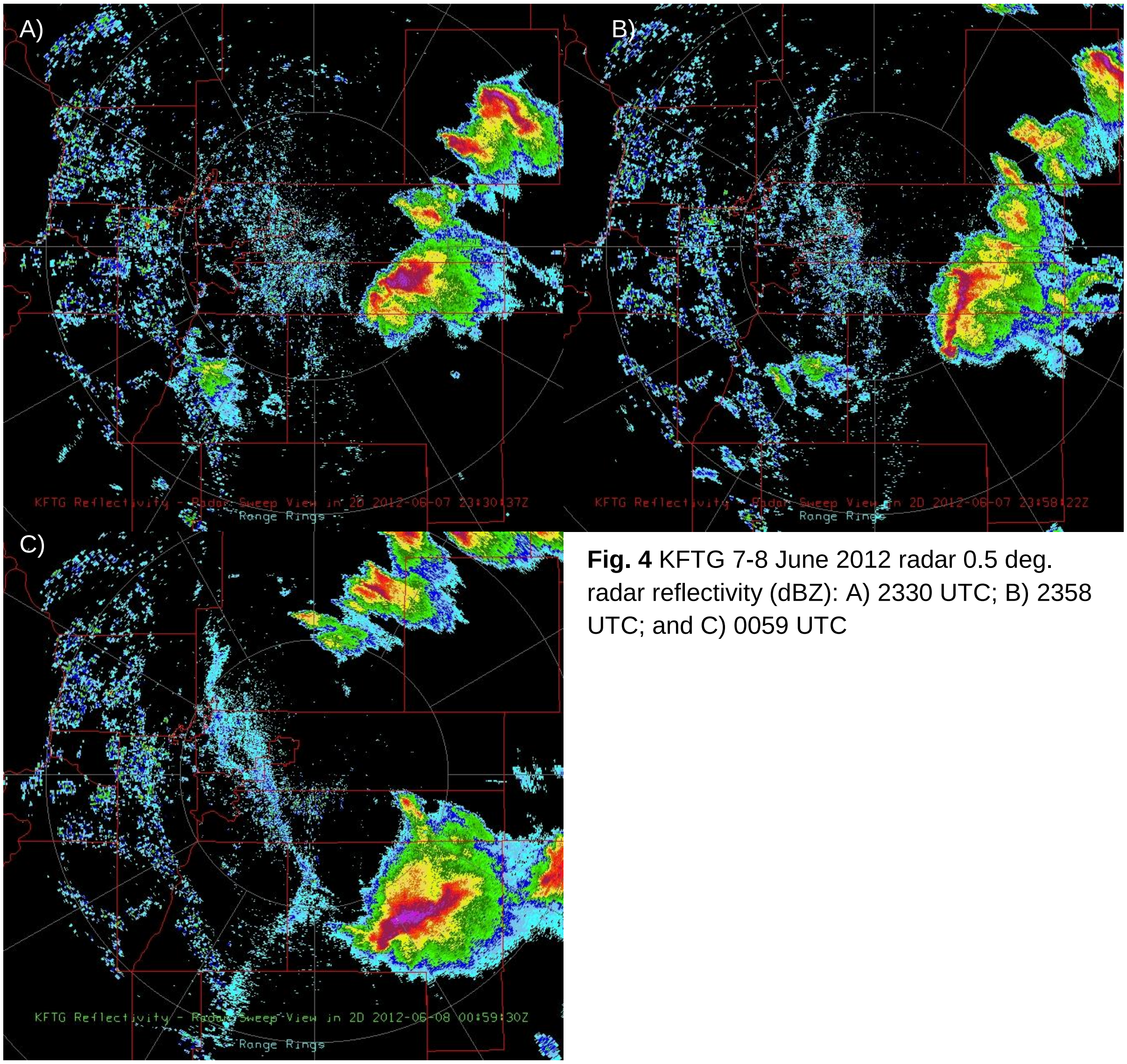

Fig. 4 KFTG 7-8 June 2012 radar 0.5 deg. radar reflectivity (dBZ): A) 2330 UTC; B) 2358 UTC; and C) 0059 UTC

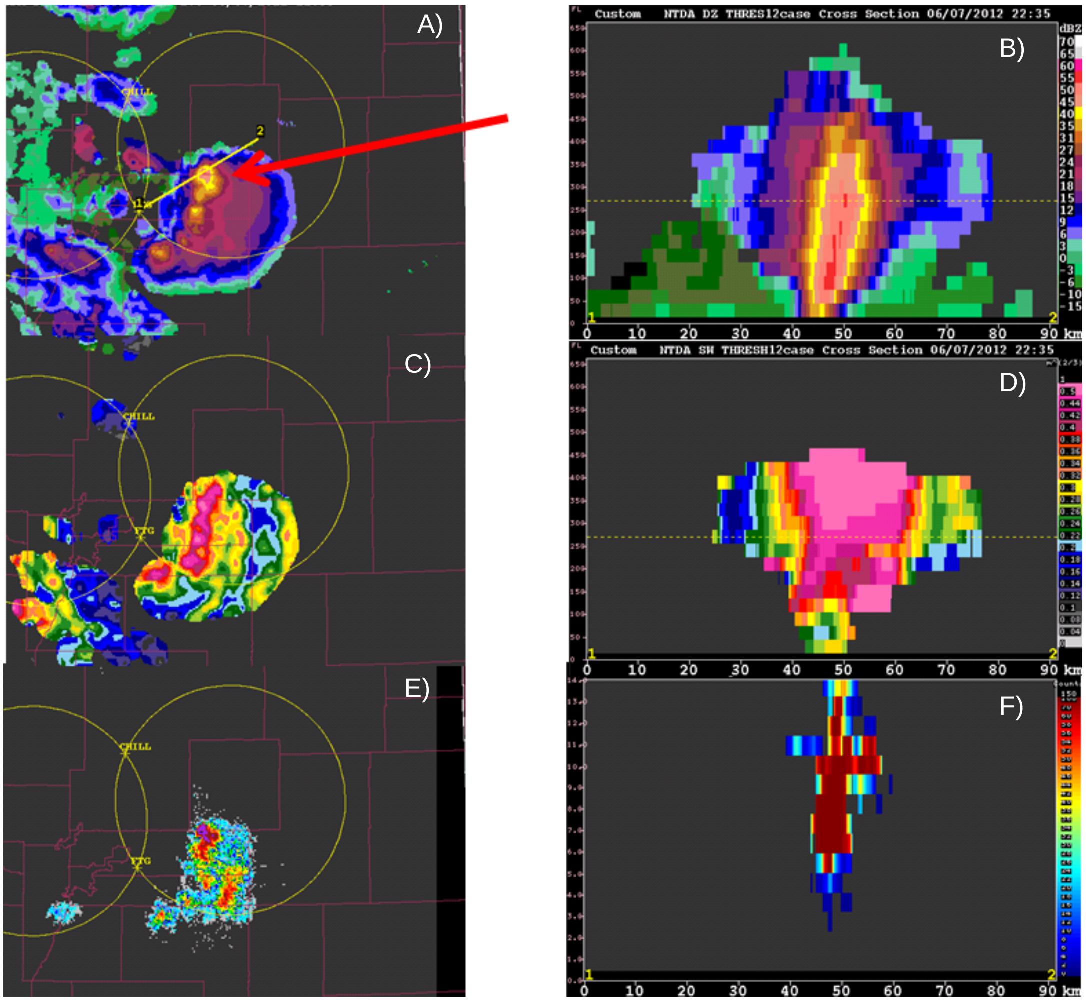

Fig. 5 7 June 2012 2235 UTC A) NTDA reflectivity at 27,000 feet which is within the mixed phase region for this storm, B) NTDA reflectivity cross-section, C) NTDA EDR at 27,000 feet, D) NTDA EDR cross-section, E) LMA flash extent, F) LMA 3D VHF source density cross-section.

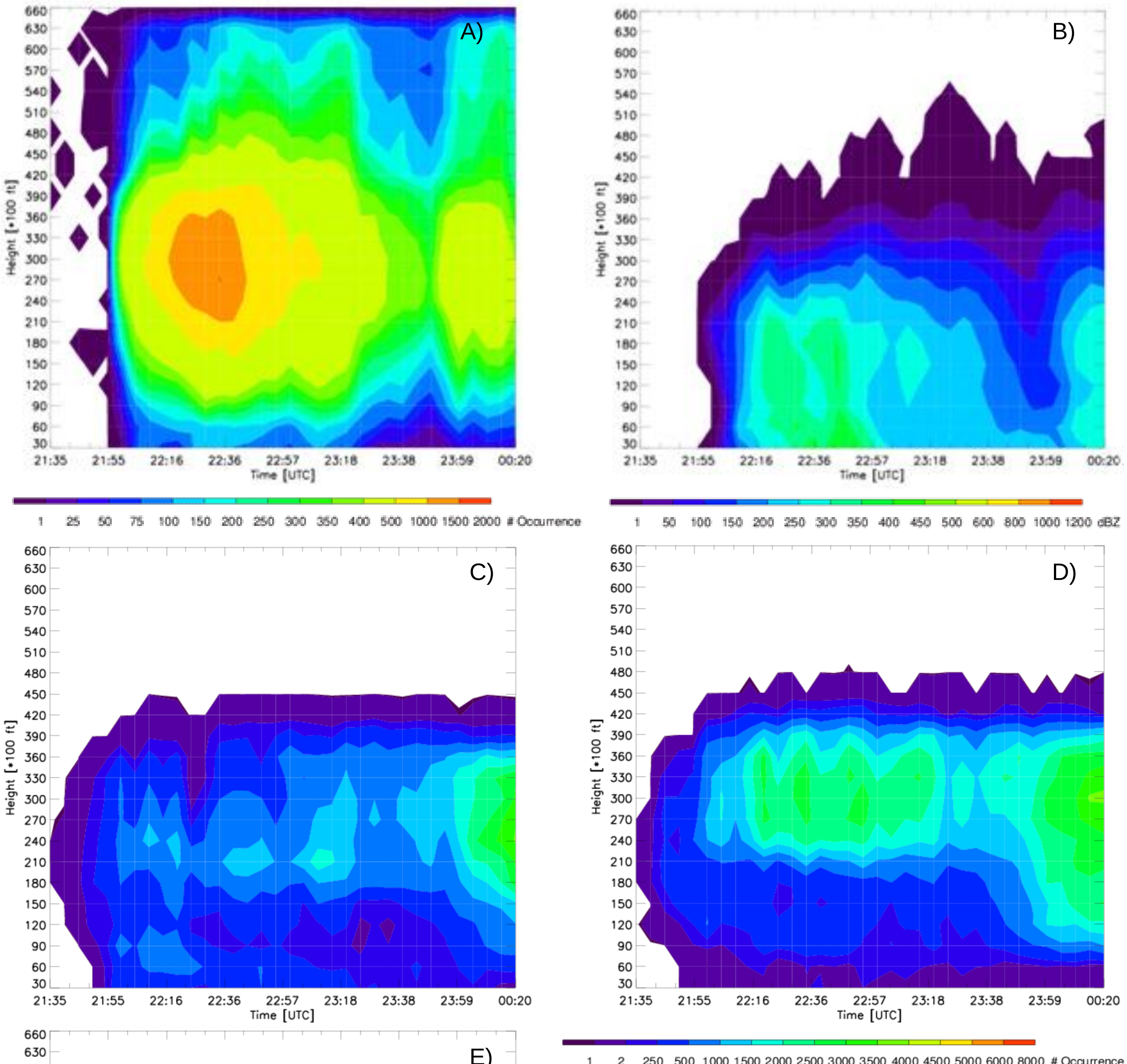

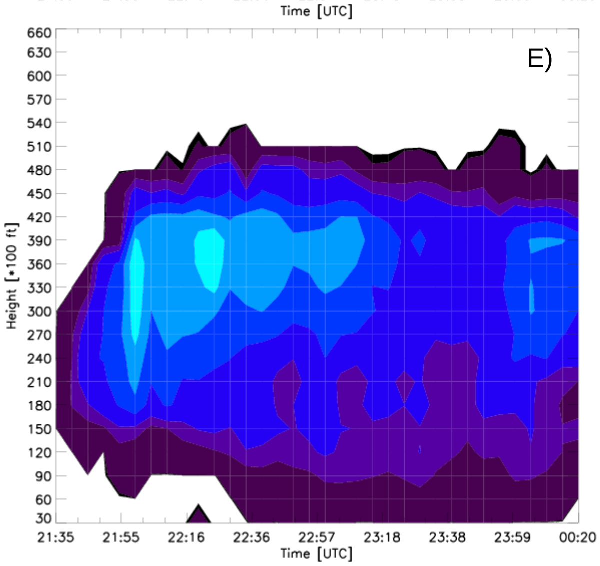

Fig. 6 Time-height plots for the northern storm normalized on storm domain, A) flash extent > 1, B) reflectivity > 35 dBZ, C) light turbulence, D) moderate turbulence, E) severe turbulence. The color bar under D) is for plots C-E.

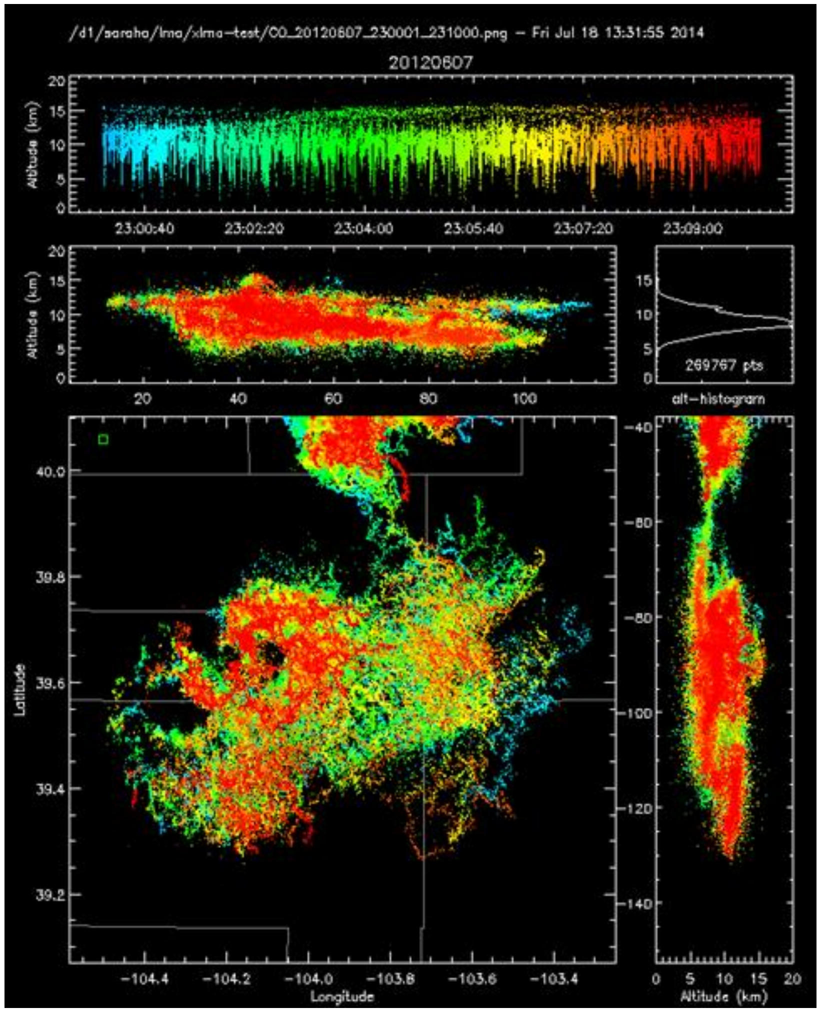

Fig. 7 LMA plot from 7 June 2012 2300-2310 UTC showing a lightning hole/bounded weak echo region. Each dot represents one VHF source and colors show time with cool colors showing older flashes and warm colors showing newer flashes.

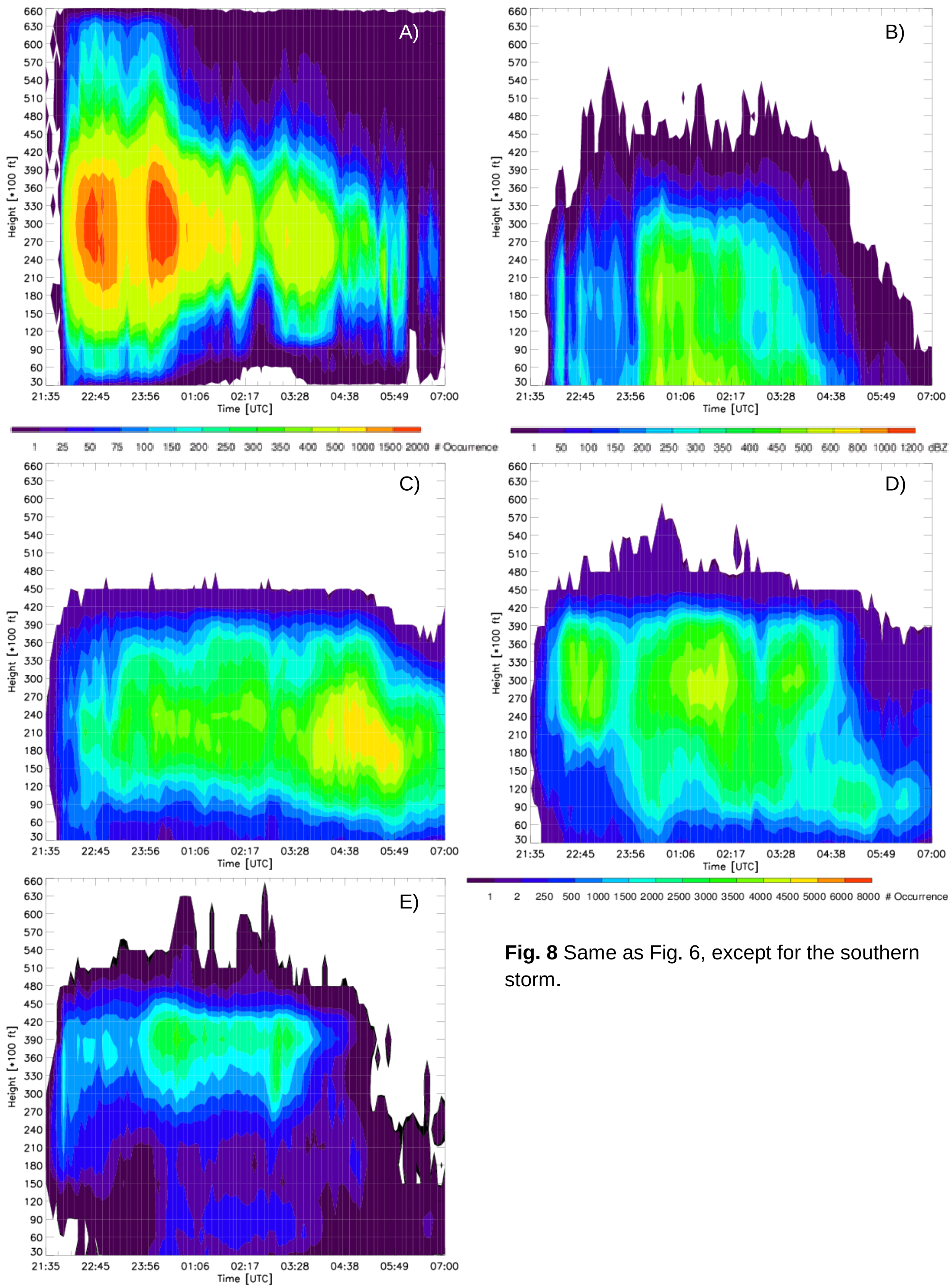

Fig. 8 Same as Fig. 6, except for the southern storm.

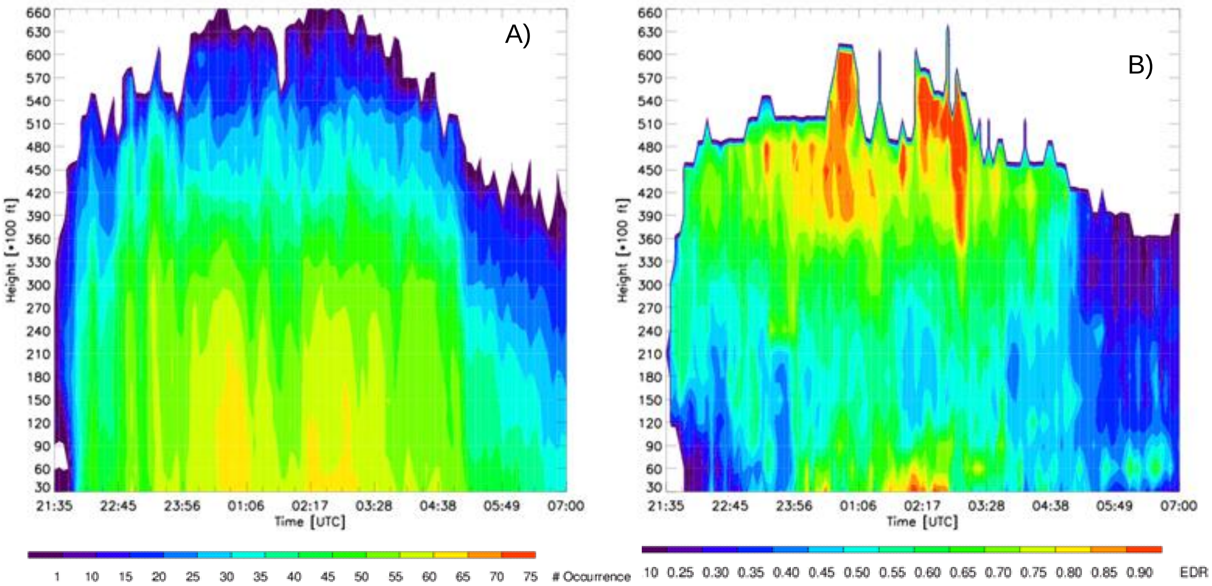

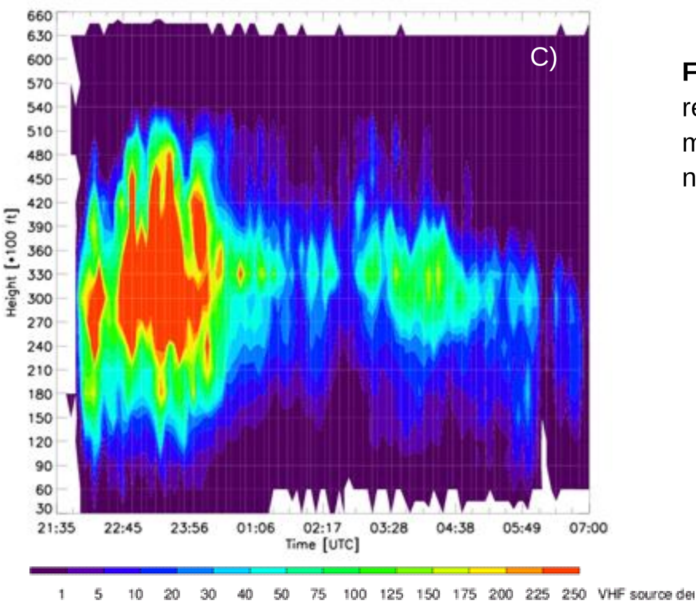

Fig. 9 The southern cell A) maximum reflectivity, B) maximum EDR, and C) maximum VHF source densities. The northern cell shows similar patterns.

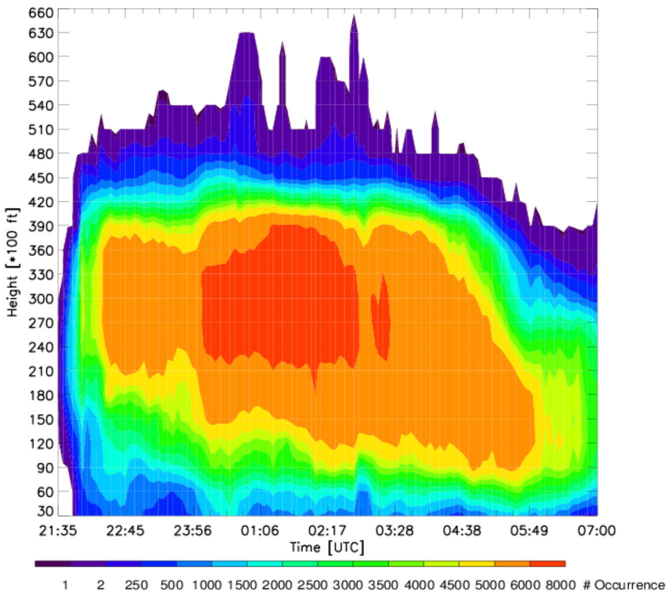

Fig. 10 The southern cell light and greater turbulence.

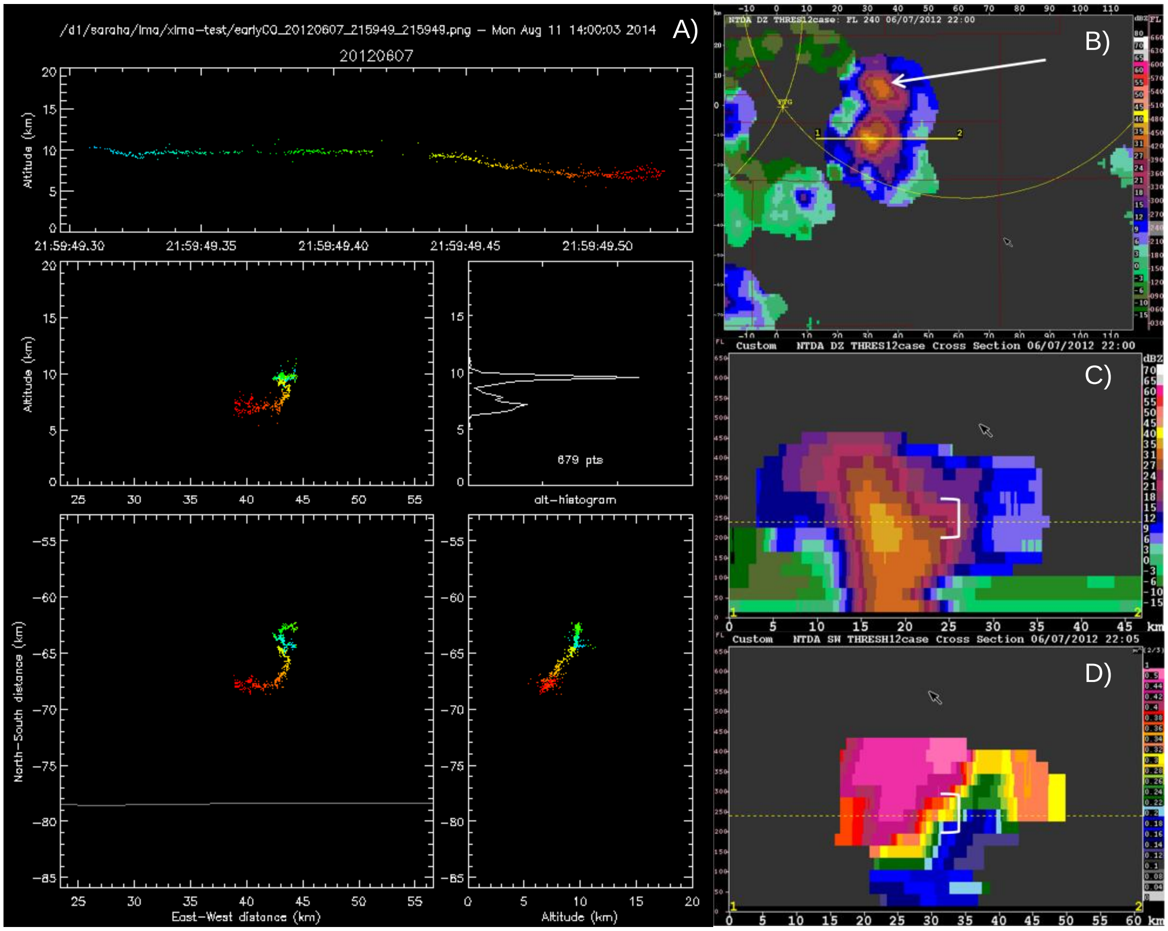

Fig. 11 Flash from 7 June 2012 215949.3-215949.6 UTC where A) LMA diagrams showing an inverse polarity structure, B) NTDA reflectivity mosaic from 24,000 ft C) NTDA reflectivity cross-section through the line indicated on plot B), D) NTDA EDR cross-section through the same area. The white arrow and brackets indicate the region where the flash occurred.

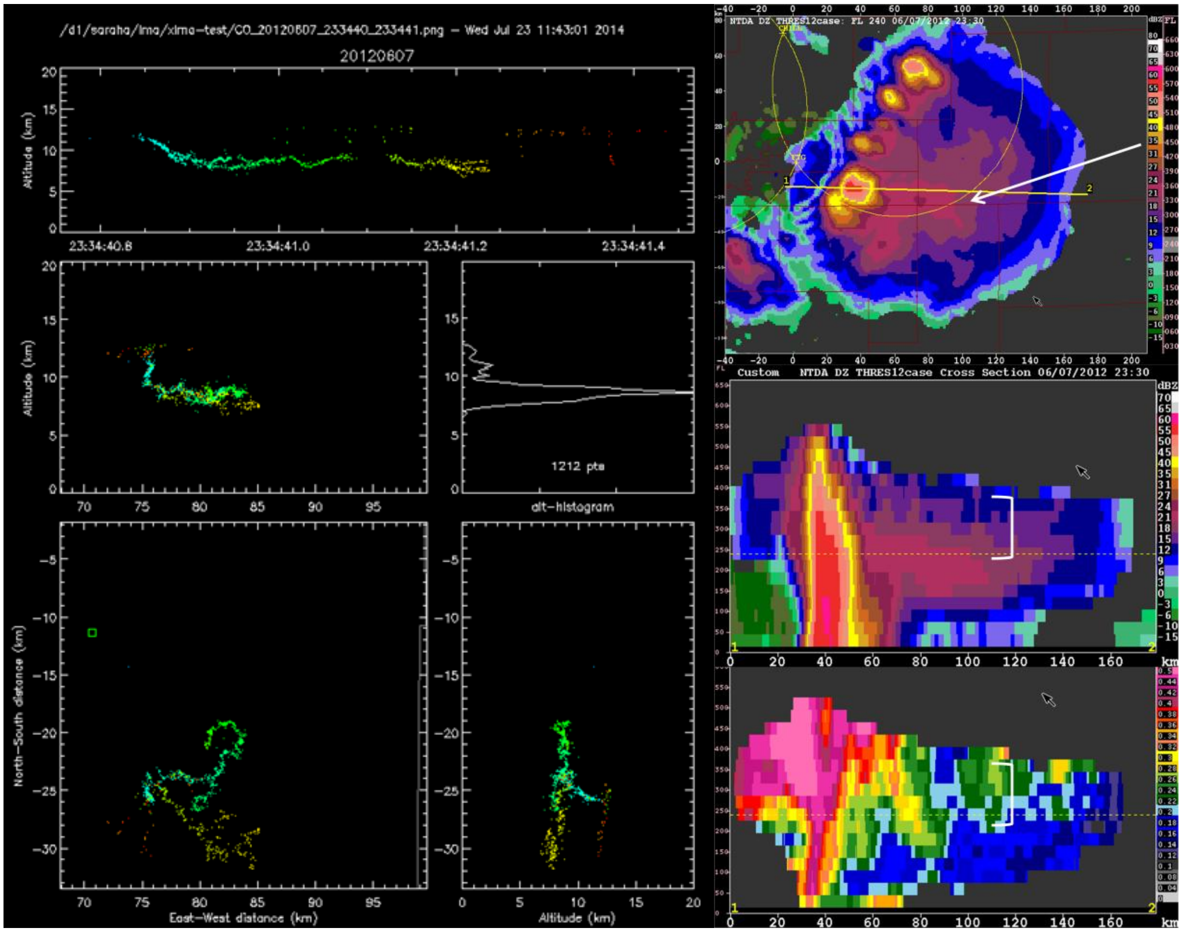

Fig. 12 Same as Fig.11 but for 7 June 2012 233440.8-233441.4 UTC

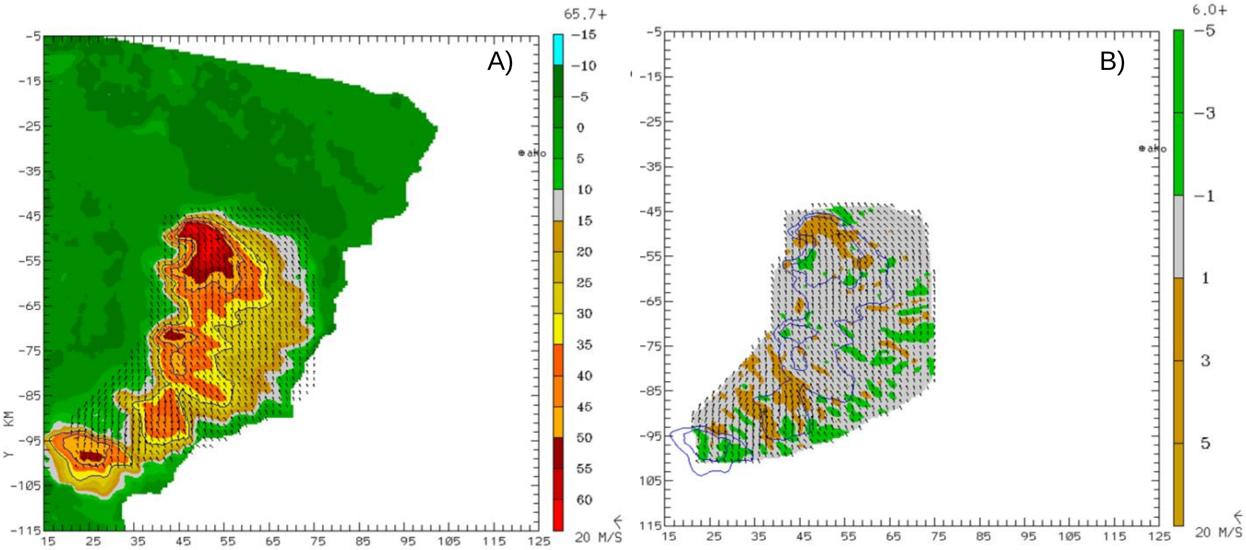

Fig. 13 2235-2239 UTC, 3 km, A) maximum reflectivity and B) convergence.

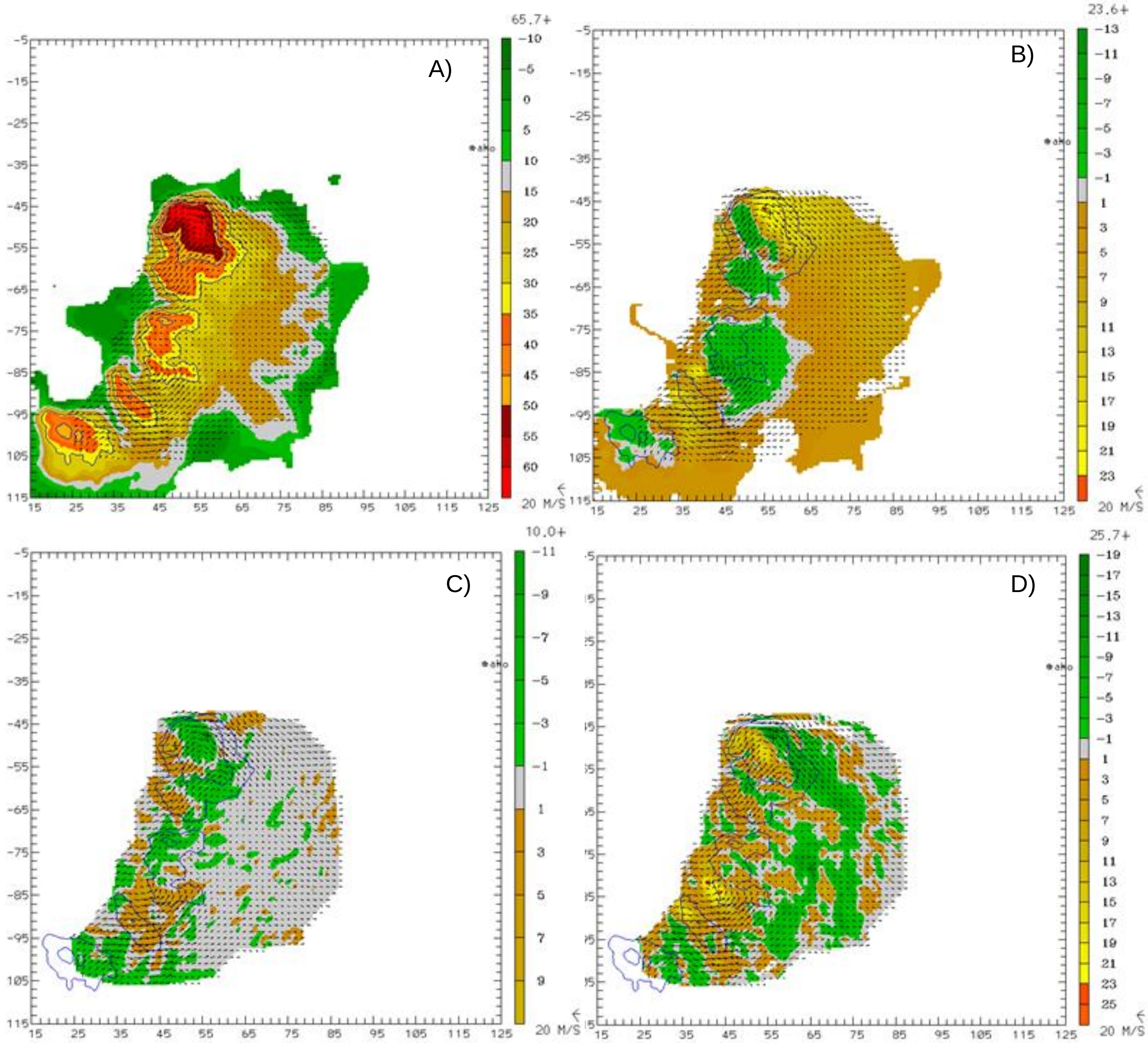

Fig. 14 2235-2239 UTC, 6.5 km, A) maximum reflectivity; B) CHILL velocity; C) vorticity; and D) W.

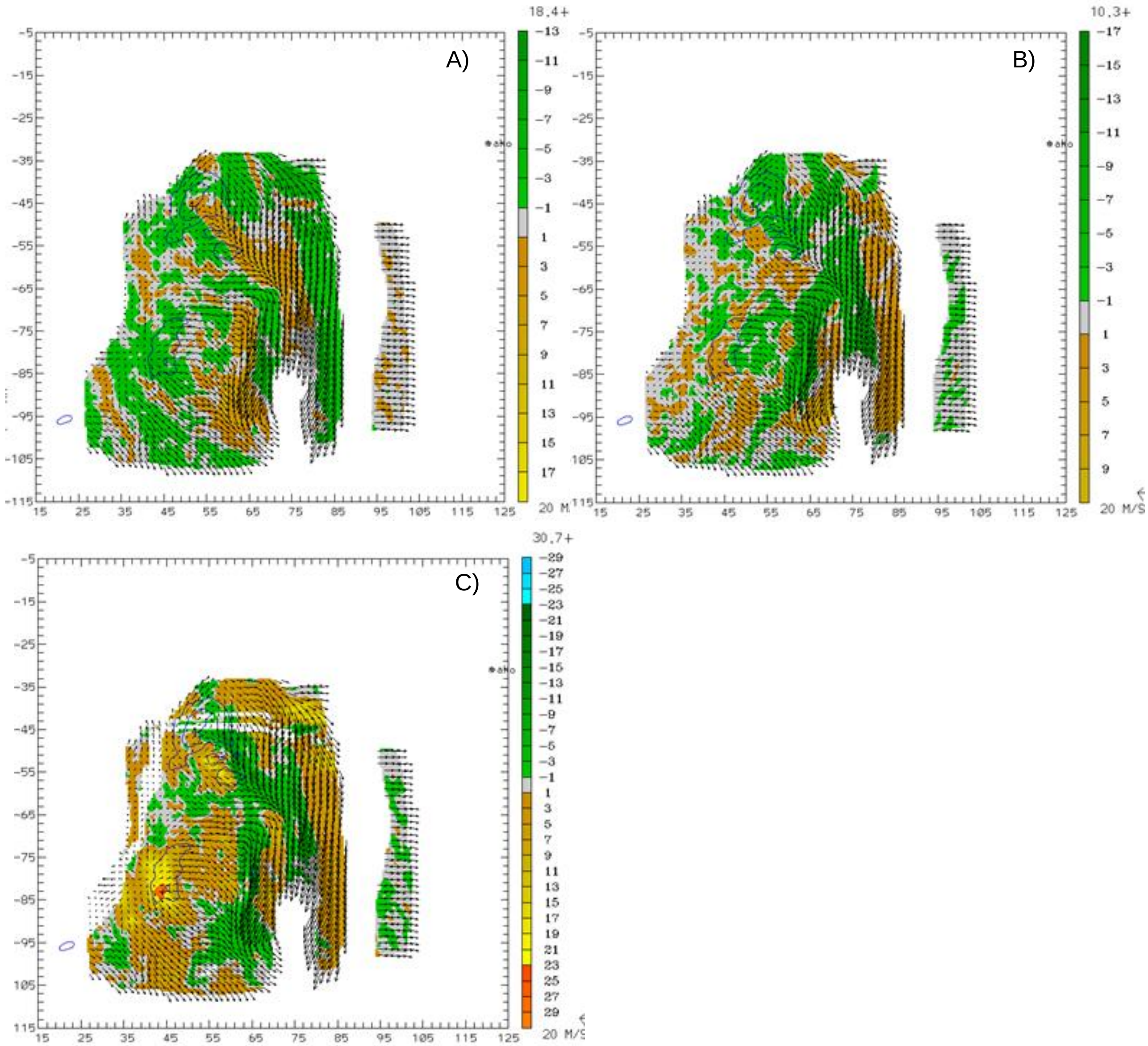

Fig. 15 2235-2239 UTC, 12 km, A) convergence; B) vorticity; and C) W.

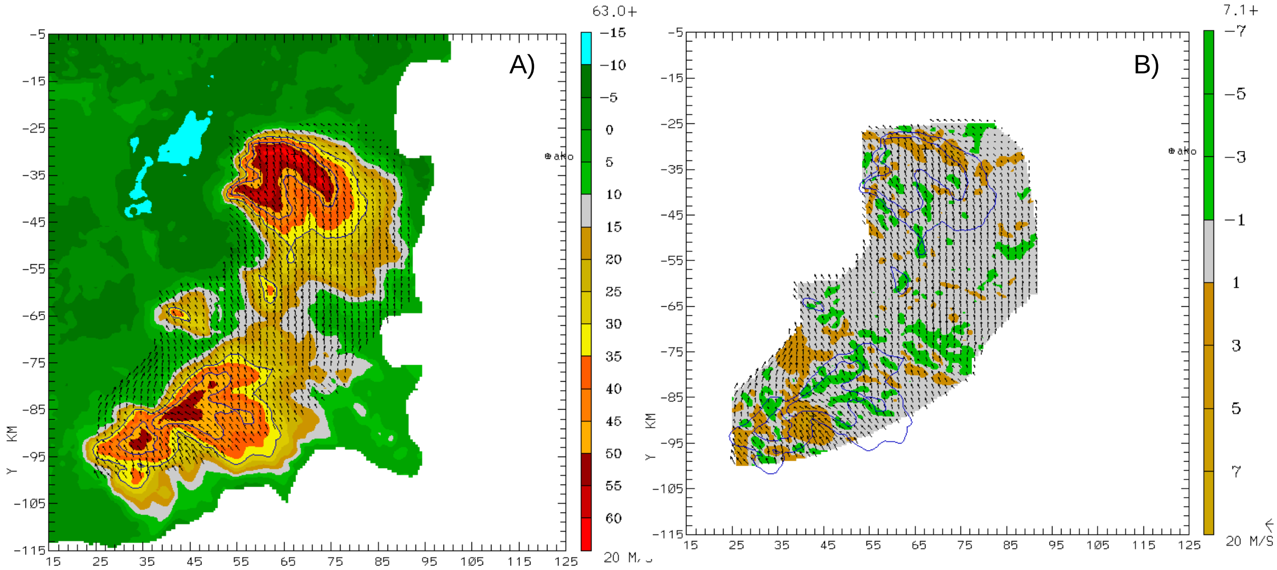

Fig. 16 Same as Fig.13 but for 2307-2312 UTC

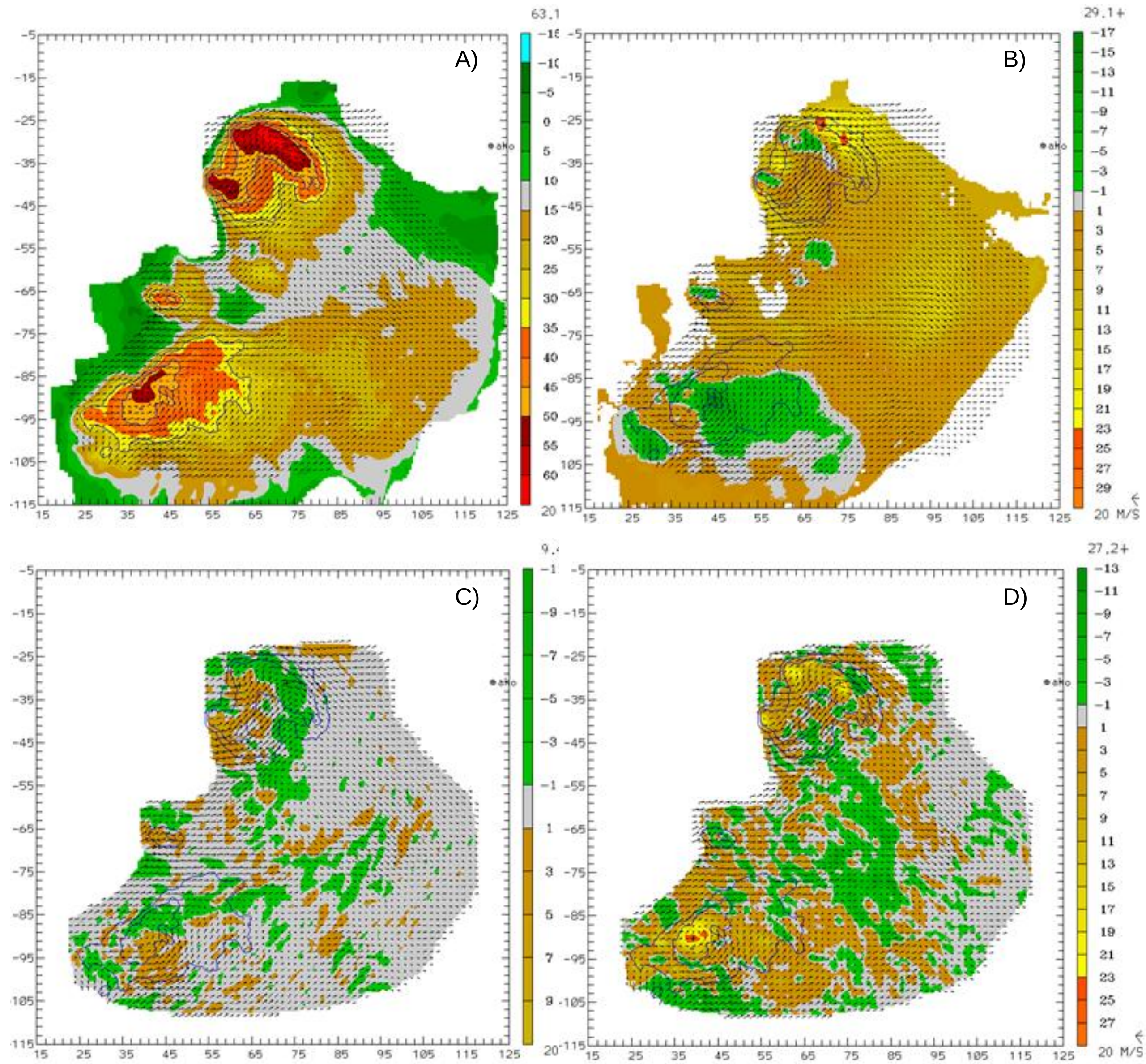

Fig. 17 Same as Fig.14, but for 2307-2312 UTC

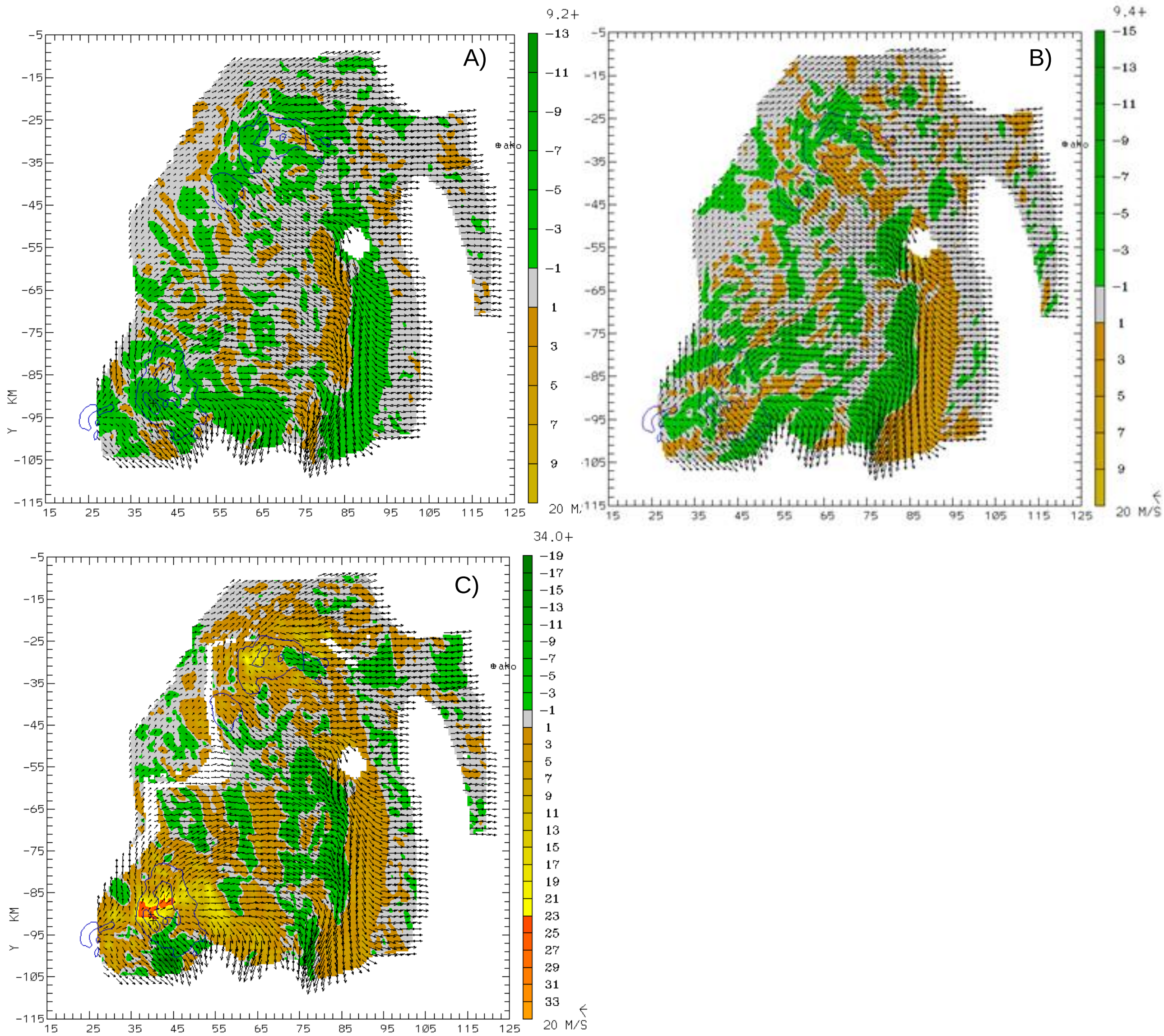

Fig. 18 Same as Fig.15, but for 2307-2312 UTC.

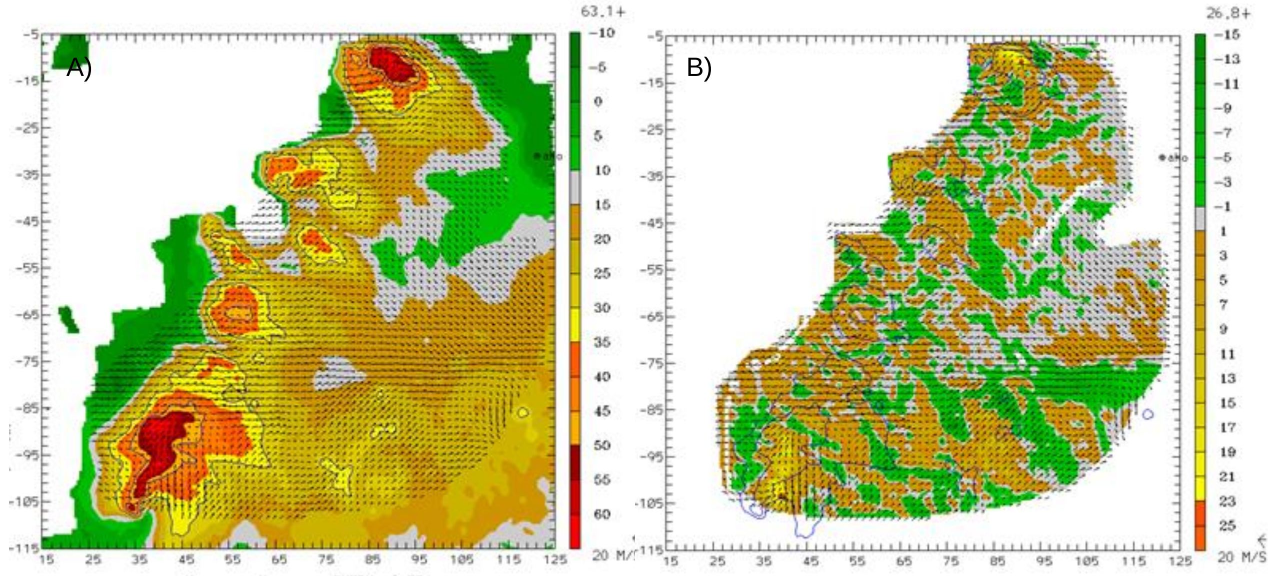

Fig. 19 2344-2349 UTC, 6.5 km, A) maximum reflectivity and B) W.

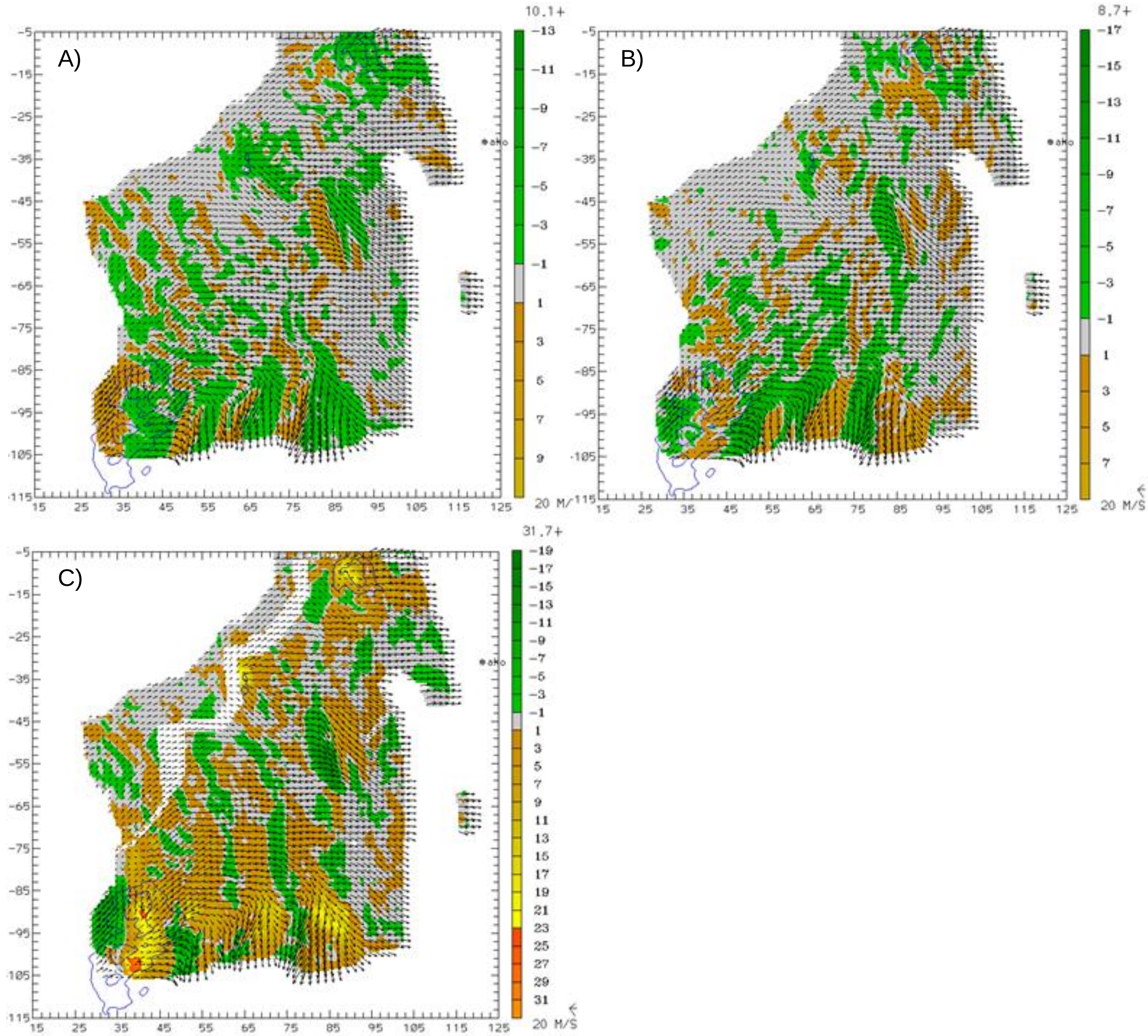

Fig. 20 Same as Fig.15, but for 2344-2349 UTC.

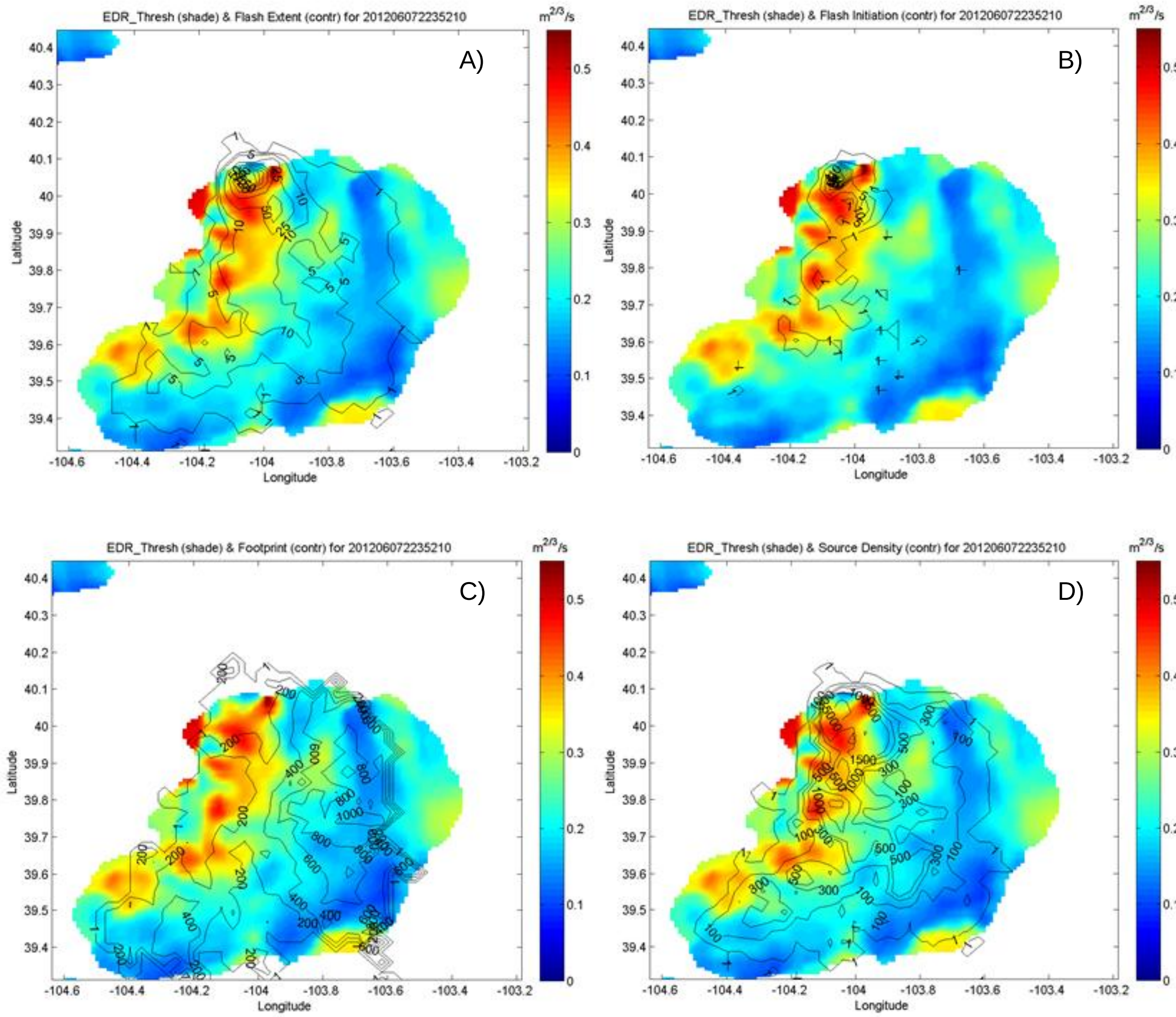

Fig. 21 A) Flash extent density, B) flash initiation density, C) mean flash area, and D) VHF source density overlaid on EDR from 2235-2237 UTC at 6.5 km.

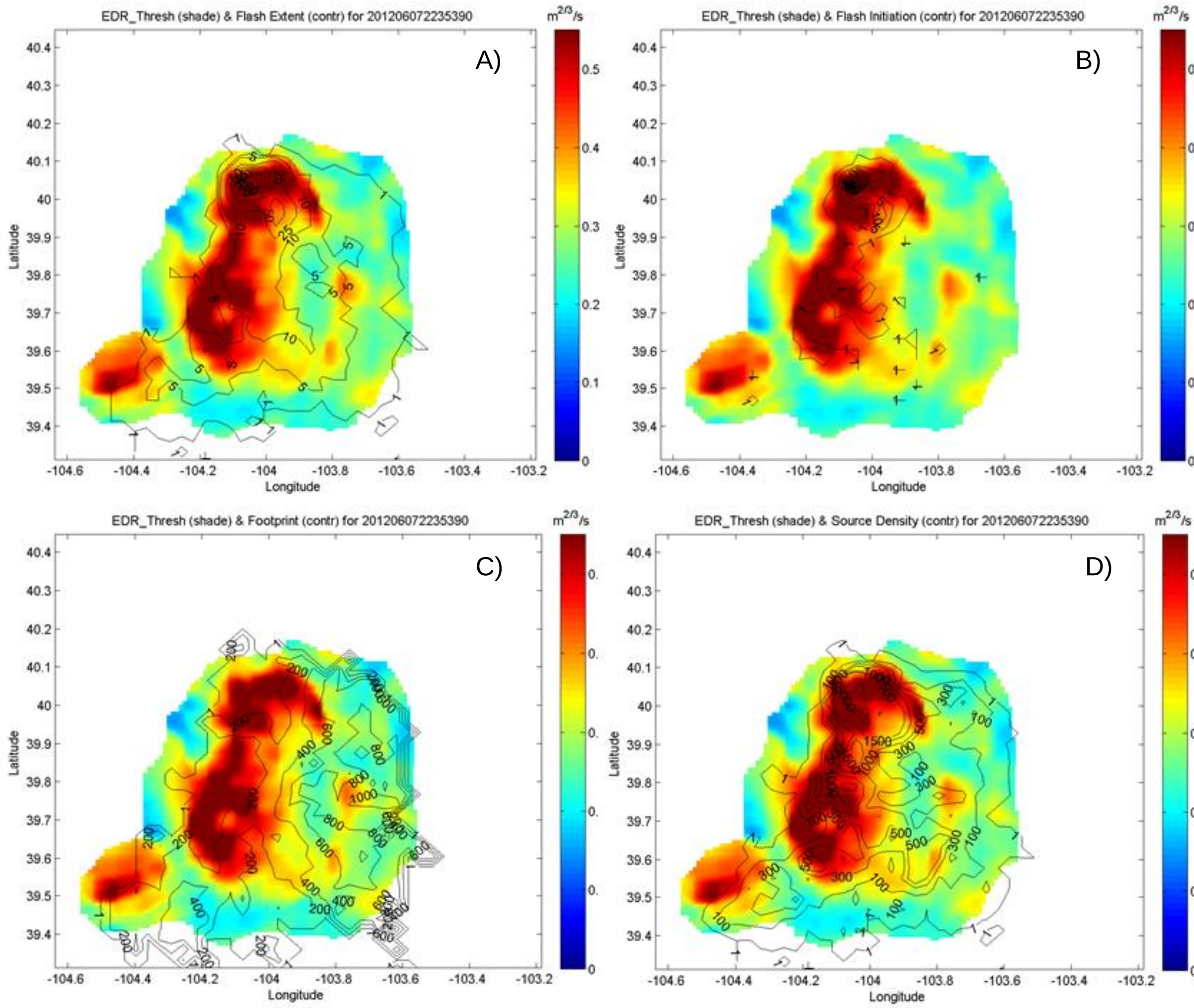

Fig. 22 Same as Fig.21 except at 12 km.

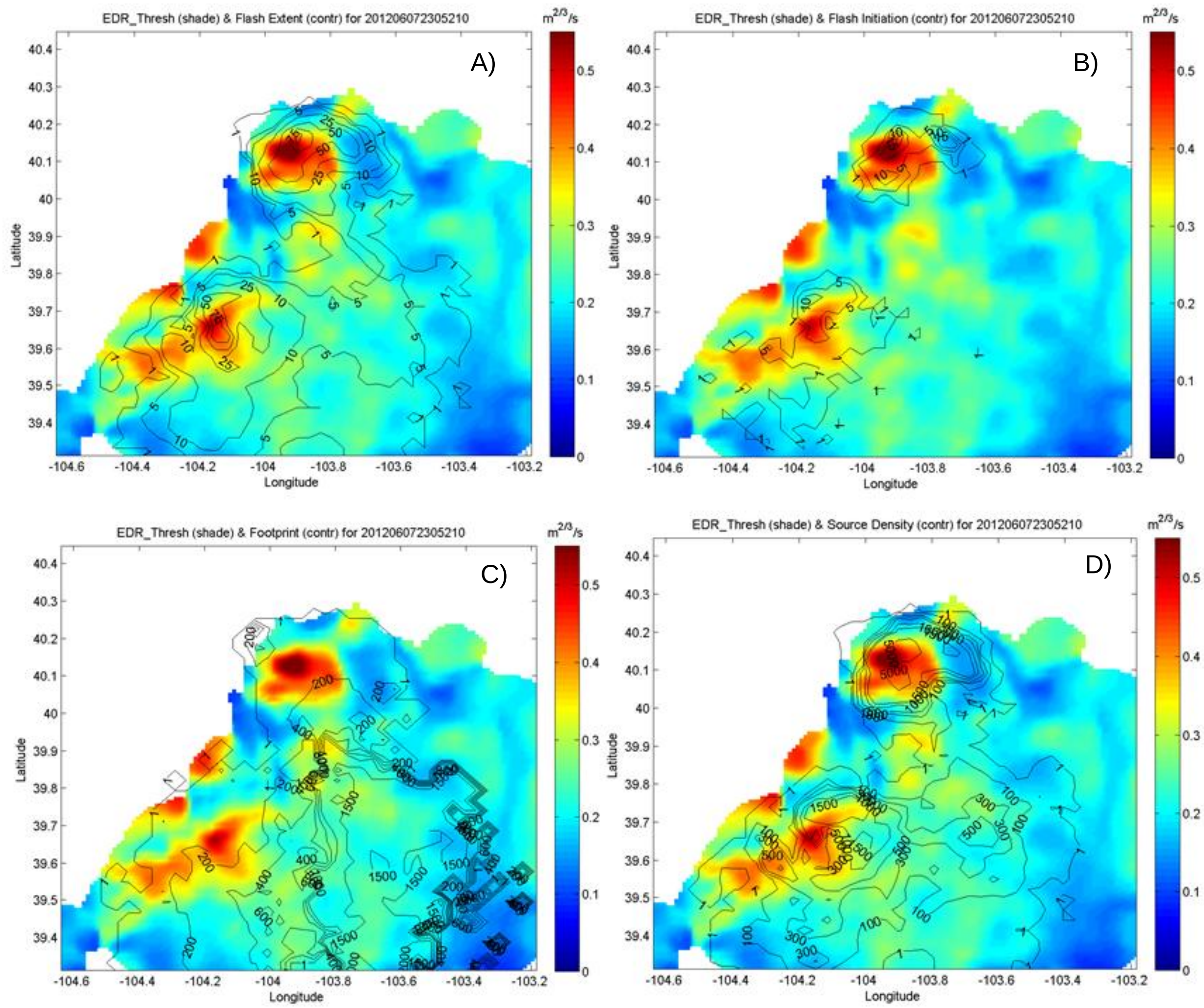

Fig. 23 Same as Fig.21 except for 2305-2309 UTC.

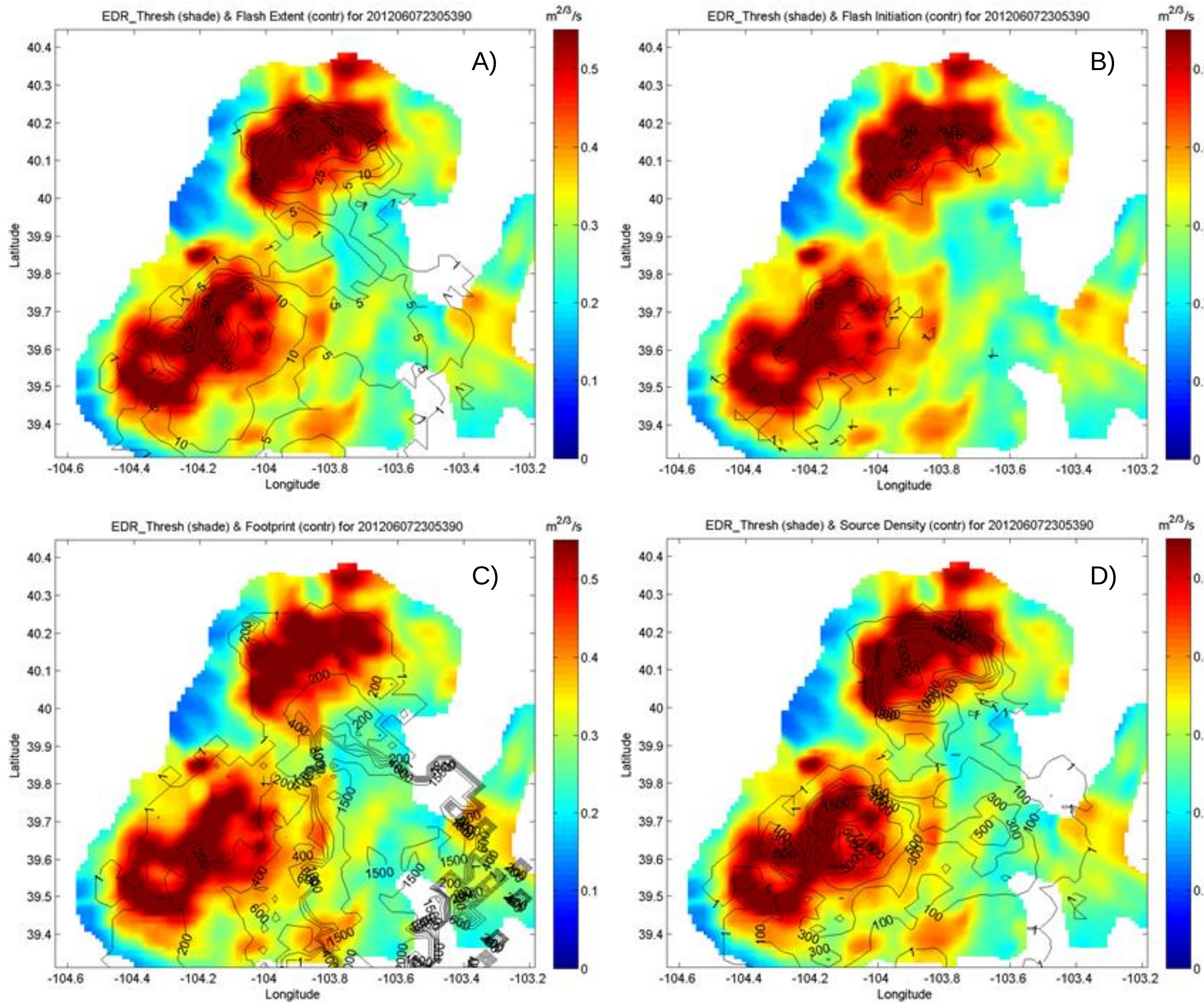

Fig. 24 Same as Fig.23 except for 12 km.

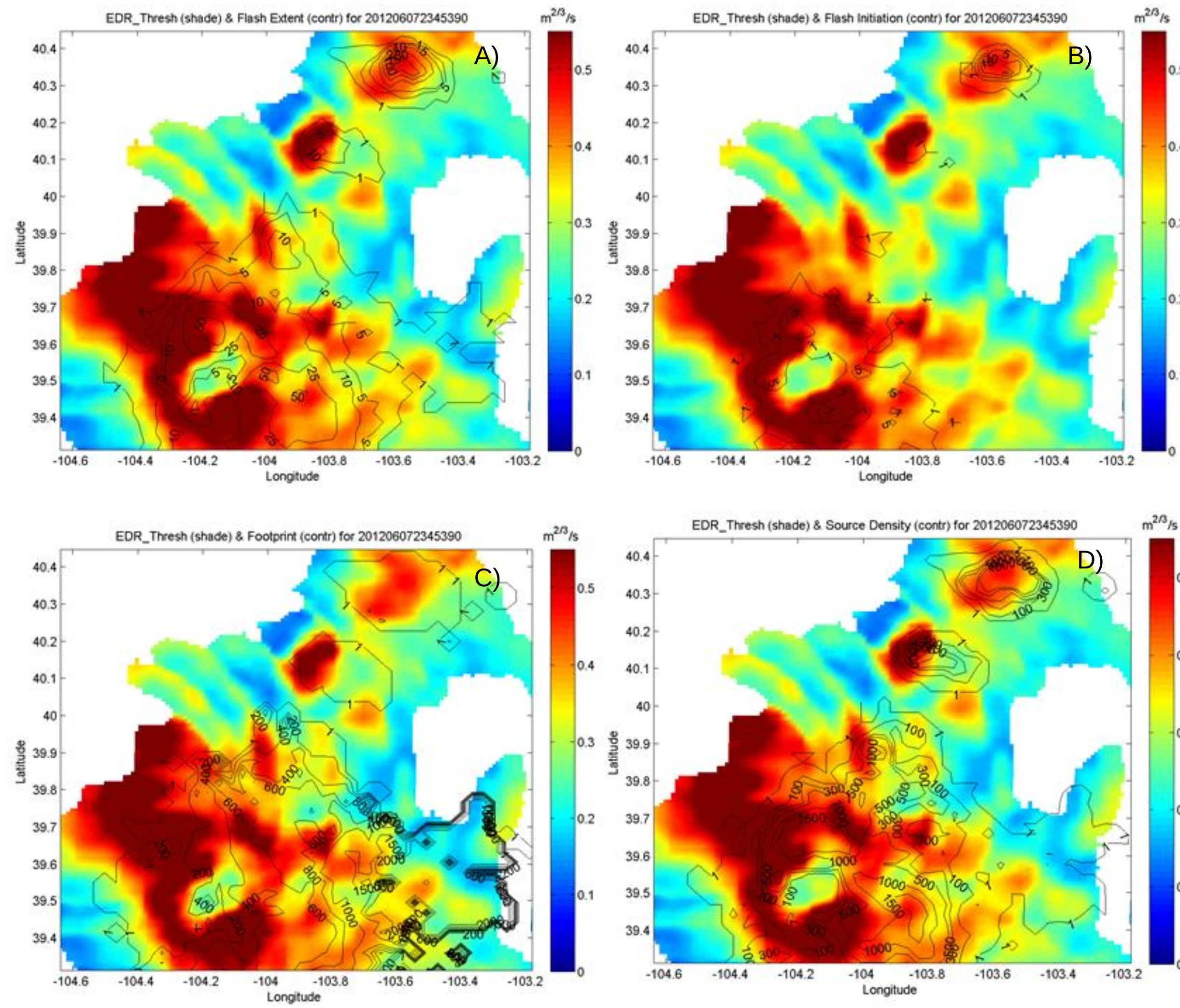

Fig. 25 Same as Fig.21 except for 2345-2350 UTC at 12 km.